

11

AD A 123 420

**RADC-TR-82-261**  
**Final Technical Report**  
**October 1982**



# **VERTICALLY FUSED FACE SHEET PERFORMANCE**

**Itek Corporation**

**Sponsored by**  
**Defense Advanced Research Projects Agency (DOD)**  
**ARPA Order No. 3503**

**DTIC**  
**UNCLASSIFIED**  
**JAN 17 1983**  
**H**

*APPROVED FOR PUBLIC RELEASE; DISTRIBUTION UNLIMITED*

The views and conclusions contained in this document are those of the authors and should not be interpreted as necessarily representing the official policies, either expressed or implied, of the Defense Advanced Research Projects Agency or the U.S. Government.

**ROME AIR DEVELOPMENT CENTER**  
**Air Force Systems Command**  
**Griffiss Air Force Base, NY 13441**

DTIC FILE COPY

83 01 17 015

This report has been reviewed by the RADC Public Affairs Office (PA) and is releasable to the National Technical Information Service (NTIS). At NTIS it will be releasable to the general public, including foreign nations.

RADC-TR-82-261 has been reviewed and is approved for publication.

APPROVED:



DORIS HAMILL, Captain, USAF  
Project Engineer

APPROVED:



FRANK J. REHM  
Technical Director  
Surveillance Division

FOR THE COMMANDER:



JOHN P. HUSS  
Acting Chief, Plans Office

If your address has changed or if you wish to be removed from the RADC mailing list, or if the addressee is no longer employed by your organization, please notify RADC (OCSE) Griffiss AFB NY 13441. This will assist us in maintaining a current mailing list.

Do not return copies of this report unless contractual obligations or notices on a specific document requires that it be returned.

VERTICALLY FUSED FACE SHEET PERFORMANCE

Harry M. Simmons  
John W. Pepi

Contractor: Itek Corporation  
Contract Number: F30602-81-C-0223  
Effective Date of Contract: 17 June 1981  
Contract Expiration Date: 15 June 1982  
Short Title of Work: Vertically Fused Face Sheet  
Performance  
Program Code Number: 1L10  
Period of Work Covered: Jun 81 - Jun 82  
Principal Investigator: Harry Simmons  
Phone: (617) 276-2356  
Project Engineer: Captain Doris Hamill  
Phone: (315) 330-3144

Approved for public release; distribution unlimited

This research was supported by the Defense Advanced  
Research Projects Agency of the Department of  
Defense and was monitored by Captain Doris Hamill  
(OCSE), Griffiss AFB NY 13441 under Contract  
F30602-81-C-0223



Accession For	
NTIS GRA&I	<input checked="" type="checkbox"/>
DTIC TAB	<input type="checkbox"/>
Unannounced	<input type="checkbox"/>
Justification	
By _____	
Distribution/	
Availability Codes	
Dist	Avail and/or Special
A	



## CONTENTS

	<u>Page</u>
1. INTRODUCTION -----	1-1
1.1 Program Objective and Scope -----	1-1
1.2 Background -----	1-1
1.3 Program -----	1-2
2. SUMMARY -----	2-1
3. DESCRIPTION OF WORK ACCOMPLISHED -----	3-1
3.1 Facesheet Blank Procurement -----	3-1
3.2 Mirror Facesheet Fabrication -----	3-4
3.3 Analytical Evaluation -----	3-7
3.3.1 Thermal Analysis -----	3-7
3.3.2 Structural Analysis -----	3-18
3.3.2.1 Math Model Description -----	3-18
3.3.2.2 Mirror Mount Analysis -----	3-18
3.3.3 Analytical Results - Performance Prediction -----	3-20
3.4 Test Evaluation -----	3-27
3.4.1 Test Summary -----	3-27
3.4.2 Test Method -----	3-31
3.5 Test Equipment and Instrumentation -----	3-33
3.6 Correlation of Test and Analytical Results -----	3-33
3.7 Results Scaled to Larger Mirrors -----	3-37
4. CONCLUSIONS AND RECOMMENDATIONS -----	3-38

## APPENDICES

A. Coating Uniformity and Mount Induced Errors -----	A-1
B. Analytical Results (Computer Output) for Low and High Flux Cases -----	B-1
C. Analytical Temperature Histories for Test 1 -----	C-1

## FIGURES

		<u>Page</u>
1-1	Alternate Methods of Producing Large Mirror Facesheets -----	1-1
1-2	Work Breakdown Structure -----	1-2
2-1	Test Orientations -----	2-1
3.1-1	Make-up of Vertically Fused Facesheet Blank -----	3-1
3.1-2	ULE Mirror CTE Distribution -----	3-3
3.2-1	Vertical Fused Facesheet Internal Stress Map at Seal Lines -----	3-5
3.2-2	One Meter Vertical Fused Facesheet - Final Fabrication -----	3-6
3.3-1	Vertical Fused Facesheet Thermal Model -----	3-8
3.3-2	Vertical Fused Facesheet Thermal Model Temperature Distribution--	3-13
3.3-4	Temperature History (Axial) -----	3-14
3.3-5	Temperature History (Radial) -----	3-14
3.3-6	Temperature History (Circumferential) -----	3-15
3.3-7	Temperature History (At Temperature Sensor) -----	3-15
3.3-8	Temperature History for Test #2 - One Meter Vertical Fused Facesheet Front Hole -----	3-16
3.3-9	Temperature History for Test #2 - One Meter Vertical Fused Facesheet - Hole Back -----	3-17
3.3-10	Temperature History for Test #2 - One Meter Vertical Fused Facesheet - Centerline 7" -----	3-17
3.3-11	NASTRAN Structural Model (Plan View) -----	3-19
3.3-12	Vertical Test Edgewise Gravity Sag Prediction -----	3-21
3.3-13	Analytical Contour Deflection for Gravity in a Sling Mount -----	3-22
3.3-14	RMS Surface Error ( $\lambda$ ) vs. Mirror Thickness ( $t$ ) -----	3-23
3.3-15	Thermal Expansion for Code 7971 -----	3-24
3.3-16	NASTRAN Contours of Distortion for Low Flux Case -----	3-25
3.3-17	NASTRAN Contours of Distortion for High Flux Case -----	3-26
3.4-1	Irradiation Test Set-Up -----	3-29
3.4-2	Test Set-Up Exterior to the DRT Chamber -----	3-30
3.4-3	One Meter Facesheet and Lamp Simulator -----	3-30
3.4-4	Spectral Radiance and Absorptance for Black Chrome Coating Irradiated by Tungsten-Argon Quartz Lamps -----	3-32
3.5-1	Thermocouple Locations for Vertical Fused Facesheet Test -----	3-36
3.6-1	Measured Peak Surface Error History of Key Components of Vertical Fused Facesheet - Test #1 -----	3-40
3.6-2	Measured Peak Surface Error History of Key Components of Vertical Fused Facesheet - Test #2 -----	3-41
3.6-3	RMS Surface Error History for Vertically Fused Facesheet Test #2-	3-42
3.6-4	Test #2 Analytical/Test Comparisons -----	3-43

TABLES

	<u>Page</u>
2.1 Aberration Amounts for Test Conditions After 100 secs.-----	2-3
2.2 Predicted and Measured Residuals After Optical Fit, 100 secs. -----	2-3
3.3-1 Thermal Model Material and Surface Properties -----	3-9
3.3-2 Measured Flux History at Reference Position (#30) -----	3-9
3.3-3 Post-Test Irradiation Heat Flux Survey Data -----	3-10
3.3-4 Schneider and TAS Determinations of Temperature History -----	3-11
3.3-5 CTE (Effective vs. Temperature) -----	3-28
3.5-1 Vertically Fused Facesheet Test Equipment List -----	3-34
3.5-2 Thermocouple Calibration for Vertically Fused Face Test-----	3-35
3.6-1 Analytical and Test Comparisons of Aberration Peaks -----	3-39
3.6-2 Analytical and Test Comparisons of Residual Errors -----	3-39

## 1. INTRODUCTION

This document constitutes the final report for the Vertically Fused Facesheet Performance program, sponsored by the Defense Advanced Research Projects Agency and conducted by Itek Optical Systems under contract to Rome Air Development Center. This report describes the work to meet the objective of this program, and includes the characterization of the facesheet sample, analytical evaluation, irradiation testing, analysis-to-test data correlation, conclusions and recommendations.

### 1.1 Program Objective and Scope

The objective of the program was to demonstrate that facesheets for very large mirrors can be made by fusing glass from different boules along a vertical seam without detrimental effects on performance in a thermally stressing environment. The scope of the effort includes analytical and experimental evaluations using Ultra Low Expansion Fused Silica (ULE)<sup>TM</sup>.

### 1.2 Background

Corning Glass Works is the only supplier of high quality, low expansion glass for large optical mirrors in the U.S. Currently, Corning is not able to make large face plates from a single boule of glass if those plates are to be larger than 3.3m in diameter. Corning has suggested developing a larger than standard boule (greater than 3m) and flowing it out to the required diameter. This process however, is time-consuming, expensive and wasteful of glass. Corning has another process for fusing glass from different boules along vertical seams to make large pieces of glass, but this was always considered to increase performance risk because of boule-to-boule variations in the properties of ULE. Recently Corning has increased the quality control for ULE production, and as a result there is much less boule-to-boule difference in the glass. This means it may now be feasible to vertically fuse ULE and still meet the performance specifications. Some of the issues and advantages to these alternate methods of producing large mirror facesheets is shown in Figure 1-1. This study will determine if vertically fused ULE from different boules can meet the performance requirements for high flux systems like the LODE Advanced Mirror Program - Segmented (LAMP-S).

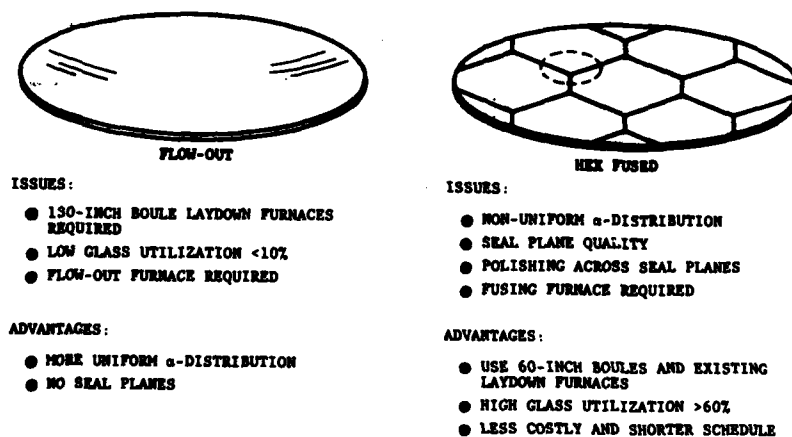


Figure 1-1 Alternate Methods of Producing Large Mirror Facesheets

### 1.3 Program

To achieve the objective of the Vertically Fused Facesheet Statement of Work, a 9-month study was conducted by Itek Optical Systems. This study was structured around three principle tasks. One task involved the thermo-structural analysis of a one meter diameter test sample of a LODE-type facesheet subjected to simulated LODE-type thermal stressing condition. A second task included the design, fabrication and material characterization of the one meter facesheet sample. The mirror is made from three pie-shaped segments fused together from two different boules of ULE™ glass. The third task required the finished mirror to be tested optically under thermal flux loadings and the results correlated with analytical predictions. The work breakdown structure for the study is shown in Figure 1-2.

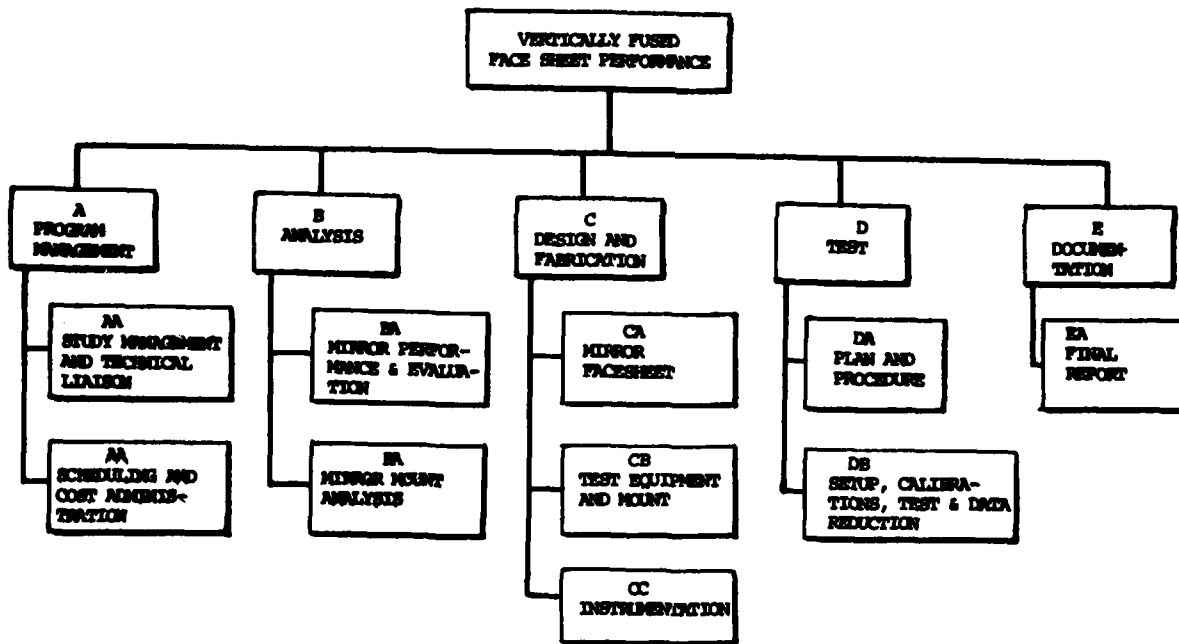


Figure 1-2 Work Breakdown Structure

## 2. SUMMARY

This study evaluates the performance of a fused segmented facesheet mirror used in actively controlled mirror systems. The one meter diameter by 20mm thick facesheet design is such that the mirror is made up of three pie-shaped segments fused together from two different boules of ultra-low expansion fused silica (ULE<sup>TM</sup>). The mirror segments were purposely mismatched for expansion properties, two segments having negative coefficients of thermal expansion (C-T-E) and the third having positive values. The facesheet C-T-E properties were characterized in detail both radially and axially. The total range of C-T-E variation was from  $-0.018 \times 10^{-6}/^{\circ}\text{C}$  to  $+0.012/^{\circ}\text{C}$ . Also, internal stresses along the seal lines were measured and stresses up to 129 psi were indicated. During optical surfacing operations of generating, grinding, edging, and polishing, the vertical seal planes offered no problems or impediments to manufacturing operations. An interferogram of the final figure of the facesheet showed no discontinuity or effects at the seal lines.

In order to evaluate the mirror optical performance during incident flux loading, two thermal tests were run. The first utilized a low flux level with the mirror oriented as shown in Figure 2.1, while the second utilized a higher flux level with the mirror rotated 180°. Both flux asymmetries and mirror segment CTE biases were investigated.

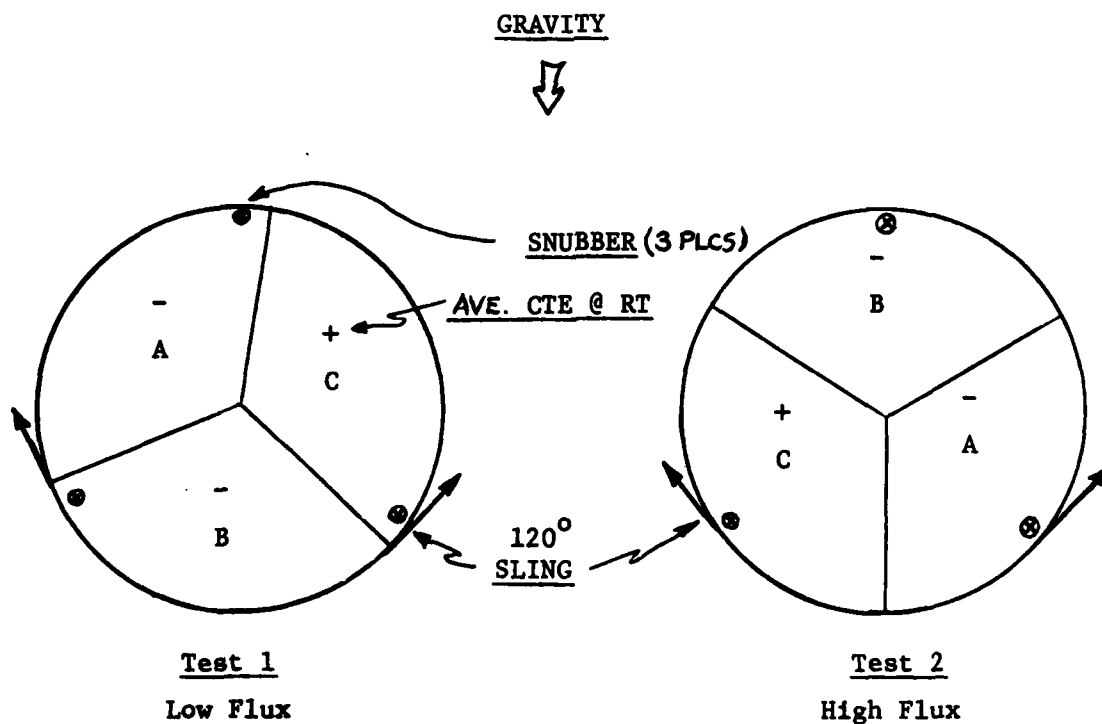


Figure 2.1 Test Orientations

An understanding of the performance characteristics of fused mirror technology was gained, which can be important to large aperture systems. Thermal math model analysis results were correlated with measured test temperatures. Analytical temperature data for rapid heat-up transients were incorporated into a detailed NASTRAN structural model to predict various surface deflections. By comparing these analytical predictions with measured test deflections using interferometry, an understanding of vertical seal lines and variations of coefficient of thermal expansion to performance was gained.

To accurately predict the distortion of the facesheet under thermal load, it was important to

- 1) understand the gravity test sag of the thin facesheet so as not to mask out the thermal errors;
- 2) understand the mirror mount induced loadings during irradiation which might significantly distort the surface relative to the thermal error; and
- 3) incorporate not only the Corning room temperature measured C<sub>T</sub> variations but also account for thermal strain variations over the entire region of the thermal environment.

The detailed results of how these were evaluated and incorporated into our math model are discussed in the body of this report. In light of the analyses, it was concluded that the results of the second thermal test, in which a higher flux load was imposed upon our facesheet, could be more readily correlated. This is so in that the total thermal strain is nearly three times higher than in the first, lower flux test, thereby providing a significantly higher signal relative to mount and noise error.

With reference to these tests, it is pertinent to note the amounts of measured aberrations relative to those predicted by the structural math model (aberrations predictions are obtained by post processing of the NASTRAN displacements thru the Itek Optics Performance Prediction Program). Such values are summarized in Table 2.1 for the case of 100 secs irradiation. There is an excellent analytical correlation in both magnitude and sign for the measured focus (power) term for the latter test, both yielding on the order of three surface waves convex (mirror flattening) power error. There is also a good correlation of predicted comatic angle of error between tests one and two; since the mirror is rotated 180° from test to test, comatic angle moves with the mirror by this amount, as predicted. There appears, however, to be a poor correlation between the amount of measured cylinder and coma magnitudes relative to those predicted. Mount sensitivity analyses, however, as induced by the mirror sling/snubber support scheme, indicate that one wave of cylinder error is readily borne out by the mirror surface under mount loads as low as one in-lbs. of moment or one pound of radial force (as are comatic errors to a lesser degree). As later presented, purposely induced test mount errors bear out this analytical conclusion. In this regard, the summary shown in Table 2.2 is presented in which the mirror test residual after cylinder fit is compared

to the predicted residual from thermal effects alone. An excellent correlation is evidenced, both residuals of test and analysis on the order of one quarter wave rms realized for the Test 2 configuration. Higher order residuals after fourth order spherical aberration fit are also of nearly equal magnitude.

Table 2.1 Aberration Amounts for Test Conditions After 100 secs.

<u>Test</u>	<u>Aberration</u>			
	<u>Focus</u>	<u>Cylinder</u>	<u>Coma</u>	<u>Coma Angle</u>
1 Predicted	- 1.10	0.25	0.48	212 <sup>o</sup>
Measured	- 2.83	1.9	1.2	270 <sup>o</sup>
2 Predicted	- 3.1	0.6	1.8	21 <sup>o</sup>
Measured	- 3.3	2.4	0.8	55 <sup>o</sup>

Values in surface visible waves peak

Table 2.2 Predicted and Measured Residuals After Optical Fit, 100 secs.

<u>Test</u>	<u>Focus Fit</u>	<u>Cylinder Fit</u>	<u>Cylinder/Coma Fit</u>	<u>Higher Order Residual</u>
1 Predicted	.10	.08	.06	.04
Measured	.56	.23	.18	.10
2 Predicted	.30	.27	.15	.08
Measured	.52	.25	.23	.12

Values in rms surface waves, visible

Finally, as illustrated in the following sections, both analytical optical contour plots and test interferometry reductions bear out no ill effects of the fusion seal planes; i.e., the mirror behaves as if a continuous boule with CTE variations throughout.

We conclude, therefore, that we have achieved a good thermal induced error correlation between analysis and test, in terms of predicted power error match, comatic angular variations, residual fits, and absence of deleterious fusion line effects. We also conclude that the mirror is extremely sensitive to low spatial frequency mount induced error, so that a more kinematic mounting scheme would have been most desirable to negate such effects. Our mount arrangement tended to mask out self induced facesheet thermal errors, particularly at the lower flux level. Finally, we conclude that the thermal error prediction correlation for our one meter test piece is readily extrapolated to fused mirrors of larger aperture, since the analytical techniques utilized to predict errors of the test mirror are identically those utilized in performance prediction of such larger diameter facesheets.

### 3. DESCRIPTION OF WORK ACCOMPLISHED

#### 3.1 Facesheet Blank Procurement

Corning Glass Works supplied the ULE<sup>TM</sup> facesheet blank for this evaluation study. The program Statement of Work required the one meter diameter LODE-type facesheet contain at least one vertical seal plane. Also, the glass in each segment shall have variations in thermal coefficient-of-expansion consistent with those taken from different boules of glass. Figure 3.1-1 shows the vertical fused facesheet configuration used for this study. The facesheet blank consists of three equal pie-shaped segments taken from two different boules of ULE<sup>TM</sup> glass. The ULE<sup>TM</sup> glass was supplied from government inventory and was of "strut-quality" grade.

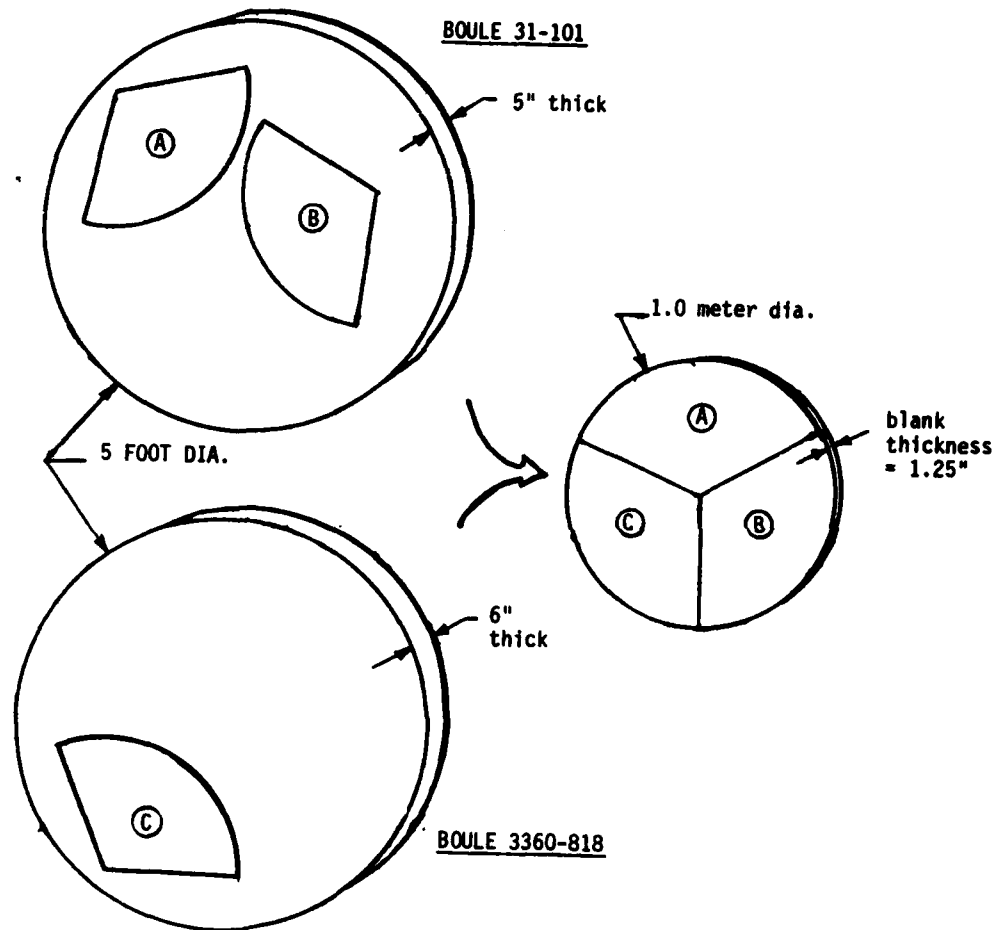


Figure 3.1-1 Make-up of Vertically Fused Facesheet Blank

The fabrication cycle for the facesheet blank can be summarized by a series of steps listed below. This section characterizes the facesheet as required by the program Statement of Work, especially step (g) where the facesheet coefficient-of-thermal expansion properties are defined.

- (a) Selected ULE segments from two boules of glass as shown in Figure 3.1-1, reviewed coefficient-of-thermal-expansion data and authorized Corning Glass Works to begin fabrication on 24 June 1981.

The coefficient-of-thermal-expansion for each boule was measured at 2-inch increments radially at three radial locations 120 degrees apart, and through the thickness in 1/8-inch increments. This CTE distribution is correlatable to the final blank and takes into account the annealing cycle by using witness samples.

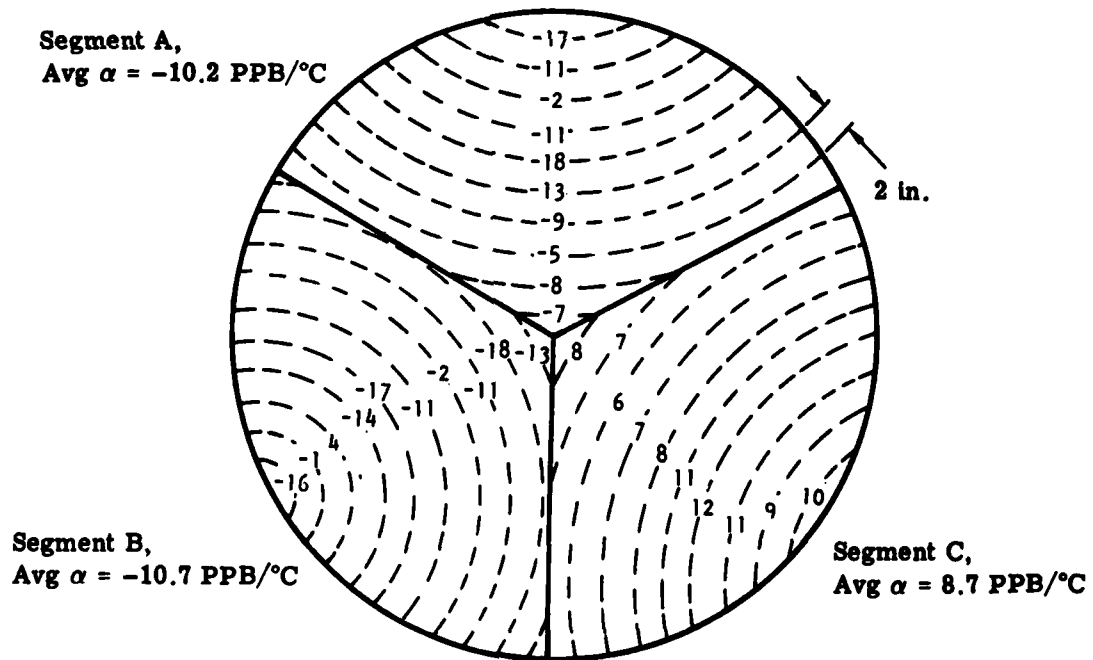
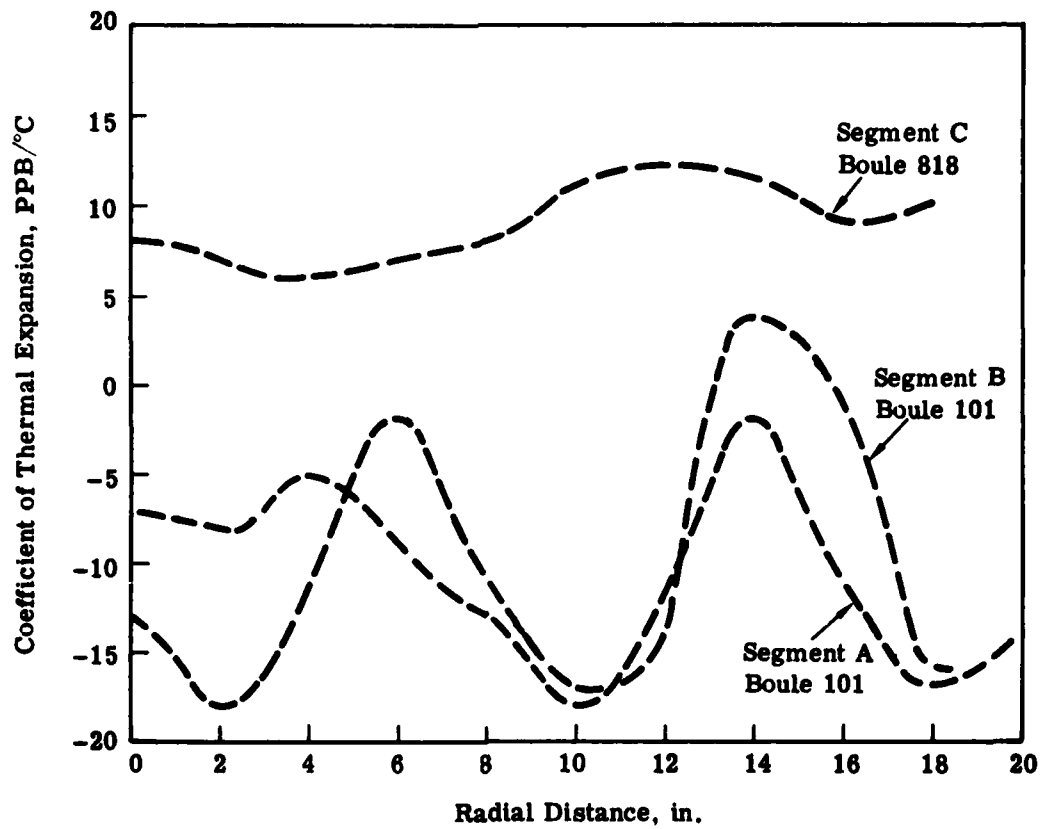
- (b) Cut-out segments. Pie-shaped segments were cut to shape using a diamond blade saw. The blank thickness of 1.5 inches was obtained by wire sawing. At this time, witness samples of glass were taken for characterizing the coefficient of thermal expansion after final anneal for the segments.
- (c) Fused segments together in a fusing furnace at temperatures of approximately 1600°C according to a controlled heat-up and cool-down cycle.
- (d) Drilled out bubble defect. The glass grade used for this study exhibited some bubbles. During the fusing process, a grouping of three bubbles elongated and extended through most of the blank thickness. It was decided to core drill out this grouping with a 3/4 inch diameter through hole. This hole, near the edge of the facesheet and 9 inches away from the nearest seal line, may be seen in some of the photographs in this report.
- (e) Slumped the fused facesheet to a spherical radius in a furnace at approximately 1600°C over a shorter period than the fusing process. The convex surface radius of curvature used was 175 inches to match existing tooling at Itek for final surfacing.
- (f) Annealed the facesheet in a furnace in what Corning Glass Works terms as a "standard" fine anneal. This process uniformly changes the CTE properties of the facesheet and that change is monitored by the witness samples noted in step (b).
- (g) KEY POINT - Characterized the facesheet coefficient-of-thermal-expansion for its final annealed state. This was done to the detail described in step (a). A summary plot of the CTE distribution is shown in Figure 3.1-2. The average area weighted CTE for each segment is:

Segment A =  $-10.2 \times 10^9 \text{ } ^\circ\text{C}^{-1}$  (PPB/°C) at room temperature

Segment B =  $-10.2$  PPB/°C

Segment C =  $+8.7$  PPB/°C

Segments A and B exhibit two characteristic peaks of CTE variations in a 20 inch (1/2 meter) radius having total amplitudes of about 20 PPB/°C. Segment C shows about one peak of CTE variation with a total variation of about 6 PPB/°C. The accuracy of CTE measurements has been stated by Corning Glass Works to be about 1 to 2 PPB/°C. There was no effort in this program to better match these segments for more uniform CTE distributions. In fact, some differences were intended in order to provide some measurable thermo-deflections.



- 1-m-diameter  $\times$  20-mm-thick fused facesheet
- $\Delta\alpha$  through the thickness =  $\pm$  PPB/°C
  - All  $\alpha$  values at 20°C

Figure 3.1-2 ULE Mirror CTE Distribution Based on Measurements of Vertically Fused Facesheet

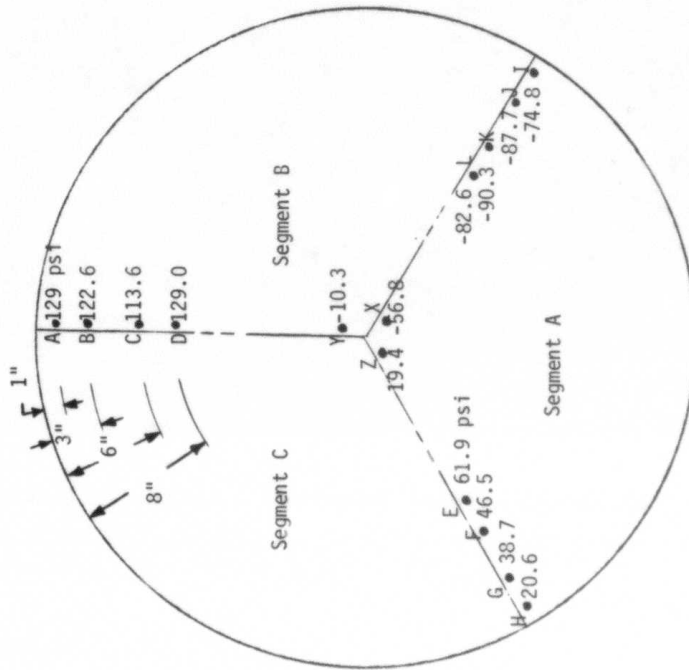
In manufacturing large facesheets, it is quite possible to provide segmented mirrors having better CTE matching than this facesheet to provide better optical performance under thermal stressing conditions.

- (h) Corning delivered the facesheet blank to Itek, October 6, 1981 on schedule, 15 weeks after start of fabrication and that includes a 4 week plant shut down.

### 3.2 Mirror Facesheet Fabrication

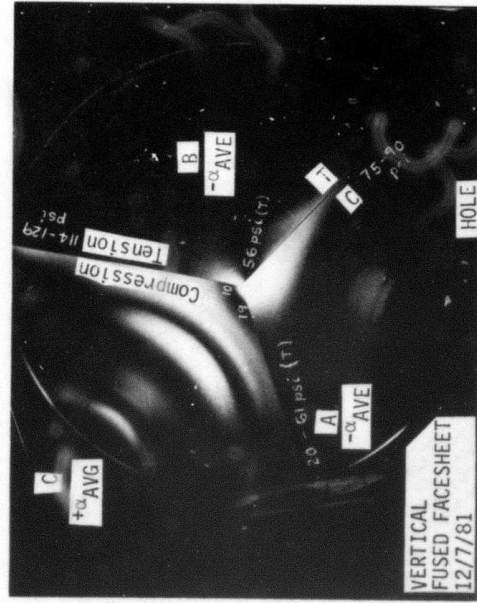
Mirror fabrication involves a number of optical surfacing steps to make the facesheet blank into a mirror of sufficient quality for thermal loading evaluation. These steps which were done at Itek will be outlined below.

- (a) Inspection and Clean-up - The facesheet passed incoming inspection October 8, 1981. The blank was given to optics to carefully clean-off a thin crystalline layer of glass on the center area of the concave side.
- (b) Grind Convex Surface - The convex surface was ground to establish a "seat", using a combination grinding/support tool with a radius of approximately 177 inches.
- (c) Generate Concave Surface - The mirror blank was mounted to a support tool, using a vacuum chucking technique. A concave radius of 175.086 inches was generated into the blank with a diamond impregnated generating wheel as far as the support tool. The inner area was subsequently generated to blend into a sphere. No voids were generated in the surface.
- (d) Grind Concave Surface - Grinding was done to remove the generator marks with #30 microgrit and a grinding tool with a radius of approximately 176 inches.
- (e) Generate and Grind Convex Surface - (reference c. and d. above) The convex surface was generated to a center thickness of 0.837 inches.
- (f) Fine Grind both surfaces.
- (g) Internal Stress Characterization - At this point, the facesheet was measured at selected points along the seal lines for internal stresses. This was done by measuring the birefringence at these points using a Split Field Friedel Polarimeter, and relating birefringence readings to stress levels by using the birefringence constant for ULE™,  $3.92\mu/\text{cm}(\text{kg}/\text{cm}^2)^{-1}$ . Also, the facesheet was photographed under polarized light to show the constant strain lines (isoclines) exhibited by the facesheet. A stress map and the strain photograph for the facesheet is shown in Figure 3.2-1. There are significant internal stresses along the seal lines, especially along the seal line between segments B and C where tensile stresses of 129 psi were measured. The birefringence corresponding to 129 psi is  $3.56\mu/\text{cm}$  which is considered quite high for optical mirrors. From the strain



Viewing Concave Side

- Values shown are in psi, positive being tension and negative being compression.
- Obtained from Friedel polarimeter measurements at room temperature.



Photograph showing strain lines

- 1-M diameter blank of ULE, ground to 2.13 cm thick.
- Birefringence constant =  $3.92 \mu\text{m}/\text{cm}(\text{kg}/\text{cm}^2)^{-1}$

Figure 3.2-1 Vertically Fused Facesheet Internal Stress Map at Seal Lines



Figure 3.2-2 One Meter Vertical Fused Facesheet - Final Fabrication  
Figure (measured while back supported, optical axis vertical)

photograph, it appears that most of segment B is in tension while segments A and C exhibit a compression and tension pattern of strain.

- (h) Final Polish - The back surface was polished for stress relief. The front surface was polished to  $\lambda/2$  peak-peak surface at 632nm. Astigmatic deviation of up to  $2\lambda$  was allowed. The final fabrication figure is shown in Figure 3.2-2.
- (i) Summary - The total material removal was approximately 0.13 inches for the concave side and 0.59 inches for the convex side. The fusion lines posed no problems during any of the fabrication steps.

### 3.3 Analytical Evaluation

Analytical theory is used to predict very small, detailed deflection responses of the facesheet subjected to the thermal flux profiles of the irradiation testing of this program. The objective of the analysis is to correlate analytical predictions with test results. The analytical approach used is consistent with techniques regularly used at Itek, and employees a transient thermal program called TAS and a nationally used structural program called NASTRAN. The thermal and structural models used for this study will be described and the analytical results will be discussed below.

#### 3.3.1 Thermal Analysis

The thermal model is used to provide detailed temperature distributions in the facesheet over the irradiation periods of 20, 40, 60, 80, and 100 seconds for NASTRAN structural analysis. The detail of the model includes 135 nodes for the vertical fused facesheet and nodes for the chamber background and heat mask. The facesheet was divided axially into five thin discs of twenty five nodes each. Five nodes were included through the thickness to detail the area in the facesheet where the 3/4" diameter hole was located. Also, a one square inch area of aluminum tape (5 axial nodes) was included to simulate the front area where a thermocouple was attached. The vertical fused facesheet model is shown in Figure 3.3-1.

There were 108 radiation connections including radiation heat transfer off the front and back surfaces of the mirror to the vacuum chamber and off the mirror edge nodes to the heat mask. The chamber temperature remained constant at 70°F.

The nodes of the mirror were connected to each other by conduction radially, axially and circumferentially for a total of 358 connections. The material and surface properties assumed for the thermal model are shown in Table 3.3-1.

#### Flux Input

The flux input into the model accounted for the measured absorptance, the flux profile with time based on test flux measurement, the flux distribution with position on the mirror based on a post test flux survey.

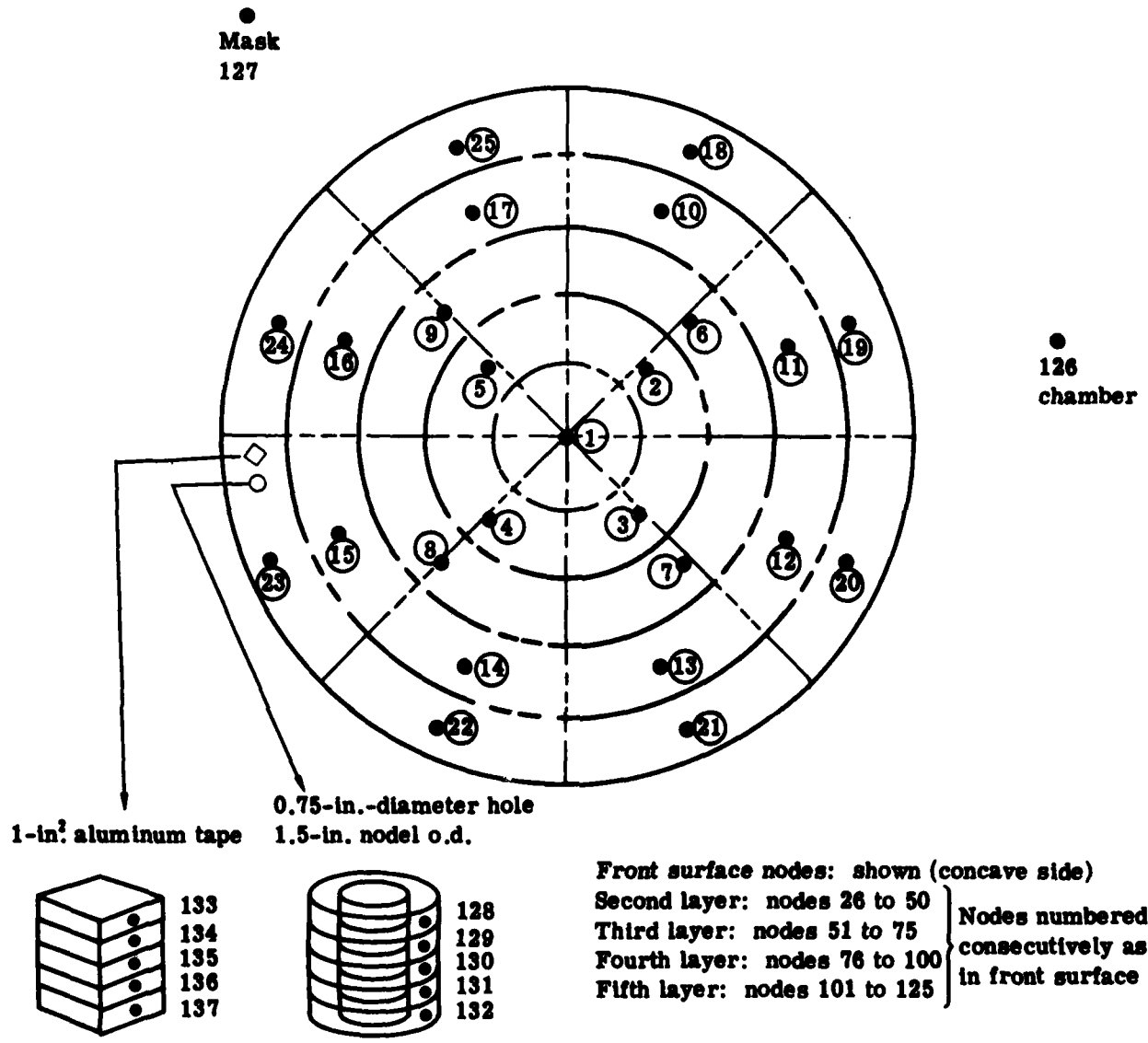


Fig. 3.3-1 Thermal Model

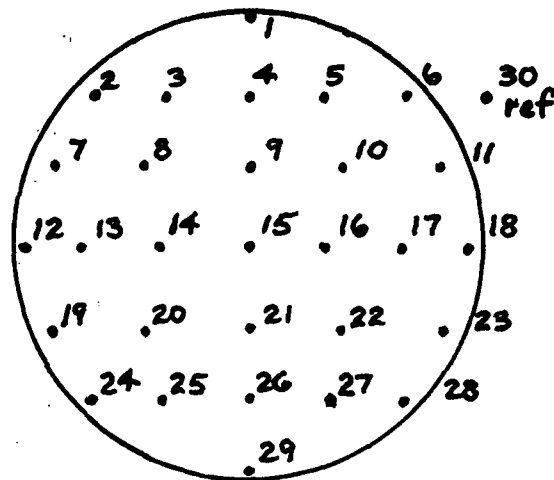
Table 3.3-1 Thermal Model Material and Surface Properties

Mirror, ULE 7971	Density	.0795#/in. <sup>3</sup>
	Specific Heat	.183 BTU/#°F
	Conductivity	.76 BTU/hr ft°F
	Emissivity, back surface	.88
Black Chrome Mirror Coating	Absorptivity (measured)	.690
	Emissivity	.824
Heat Mask, Aluminum	Density	.1007 #/in. <sup>3</sup>
	Specific heat	.2116 BTU/#°F
	Emissivity	.04
	Absorptivity	.12
Tape, Aluminum	Emissivity	.05
	Absorptivity	.17

Table 3.3-2 Measured Flux History at Reference Position (#30)

<u>Time (seconds)</u>	<u>Test #1 Flux (kw/m<sup>2</sup>)</u>	<u>Test #2 Flux (kw/m<sup>2</sup>)</u>
0	0.	0.
20	3.377	5.307
40	3.474	5.45
60	3.571	5.45
80	3.571	5.5
100	3.571	5.52

SENSOR POSITION	TEST 1 FLUX	TEST 2 FLUX
1	2.65 Kw/M <sup>2</sup>	3.33 Kw/M <sup>2</sup>
2	2.61	3.68
3	2.65	3.86
4	2.70	3.96
5	2.75	3.91
6	2.61	3.68
7	3.24	5.08
8	3.18	4.66
9	3.23	5.31
10	3.23	5.24
11	3.25	5.00
12	4.17	5.33
13	4.05	5.27
14	3.64	4.91
15	3.63	4.98
16	3.74	4.96
17	3.85	5.12
18	3.83	4.94
19	4.55	5.75
20	4.08	5.26
21	3.39	4.41
22	3.72	4.80
23	3.85	4.85
24	3.41	5.07
25	3.51	5.32
26	3.20	4.87
27	3.49	5.17
28	3.23	4.70
29	3.37	4.86
30(ref)	2.61	3.56
Positions 1-29	3.41 <sup>+33%</sup> <sub>-23%</sub>	4.77 <sup>+21%</sup> <sub>-30%</sub>



Heat flux sensor positions relative to LM mirror plane.

1. Lamp output: 8 lamps @ 440 volts.
2. Lamp-to-mirror plane distance:  
Test #1: 70 inches  
Test #2: 60 inches
3. Flux sensor conversion:  
1.0MV = 9.65 Kw/M<sup>2</sup>
4. Survey pressure: ambient
5. Flux values include mount insulation reflected energy.



Table 3.3-3 Post-Test Irradiation Heat Flux Survey Data

Table 3.3-2 shows the flux levels measured at a reference position during each test that were input into the model.

Post test flux data is presented in Table 3.3-3. From this data the effects of its position on the flux for a nodal area can be determined. The flux for 30 positions was measured in a post test survey, one of which was also measured during test. The ratio of each position's flux to this reference position's flux (the position factor), was determined for each position. A position factor for each node was determined by relating nodal locations to test position locations. The effect of reflection from the mask was considered in the above flux survey. Position factors from this data were determined similarly and this factor was included in the nodal flux load.

The average coating absorptance of 0.69 was used in the model.

The flux was applied to the front face of the mirror and into the hole. The flux load at any time for a given node in the model was the product of the reference position's flux value at that time, the nodal position factors, the nodal area, and the average measured absorptance.

#### Model Correlation with Other Analysis

The model was tested against another method of analysis, a Schneider plot<sup>1</sup>. In this analysis assumptions of constant uniform flux, insulated back face and edge, and no radiation from mirror front surface to chamber were made.

The Schneider plot presented the Fourier number, a dimensionless parameter directly proportional to time, versus a dimensionless parameter  $T = \left(\frac{k}{\delta q}\right)(t-t_0)$ , for various depths into the mirror. By reading values of T off the curve for intervals during the test, the temperature would be determined

$$t = T\left(\frac{\delta q}{k}\right) + t_0.$$

Table 3.3-4 Schneider and TAS Determinations of Temperature History (<sup>o</sup>F) of Front Nodal Surface Average Flux Cases

<u>time (seconds)</u>	<u>Test #1</u>		<u>Test #2</u>	
	<u>Schneider</u>	<u>TAS</u>	<u>Schneider</u>	<u>TAS</u>
0	70.	70.	70.	70.
20	87.1	85.7	96.4	95.1
40	95.2	94.0	108.9	108.3
60	101.4	100.6	118.7	118.4
80	106.9	106.2	127.0	126.9
100	111.3	110.9	133.9	134.4

<sup>1</sup>Schneider, Dr. P. J., Temperature Response Charts, (John Wiley & Sons, Inc. New York and London, 1963, p. 119.)

Results of this exercise are presented for the front nodes and are compared to uniform flux model determinations in Table 3.3-4.

It can be seen that the model compares within  $2^{\circ}\text{F}$  with the Schneider analysis. Reasons for the discrepancy may be due in part to the assumptions which may occur in plot reading.

A similar analysis was done for the aluminum taped section and the same agreement was seen. It was therefore assumed that the model analysis is an accurate description of the test.

#### Model Sensitivity to Test Conditions

The model's sensitivity to the test condition of a "soft" vacuum was examined. The test was conducted at 6 Torr for which there is a very small amount of air, about 1/125 of an atmosphere. For the temperature conditions, a very small convection coefficient of about  $0.005\text{BTU}/\text{HR}\text{-FT}^2\text{-}^{\circ}\text{F}$  was calculated.

To determine the effect of the test vacuum, this convection coefficient was used and a new constant temperature node representing the air in the chamber was added. The front and back surfaces of the mirror were connected to the air by convection heat transfer. It was seen that there is no significant difference between the cases with and without convection, therefore it was assumed that the convection during the test was negligible.

#### Test Data Results

The model was run for the test condition inputs as described above. A sample temperature distribution is shown in Figure 3.3-2. The temperature of both tests for each mirror node at 20 second intervals was provided for structural analysis.

Figures 3.3-4 to 3.3-6 represent axial, radial, and circumferential temperature results of Test #2 respectively. It can be seen that the largest temperature gradients occur axially, and the smallest occur radially.

The nodes plotted in Figures 3.3-7 are an axial representation of the section of the mirror under the aluminum tape for Test 2. The cooldown of these nodes is seen to be extremely slow shortly after the heating ends, unlike the other sections. This is because of the lower temperature levels reached by this area as compared with its surrounding area. The conduction between the aluminum tape section and the surrounding mirror section which is at a higher temperature halts further cooling of the aluminum tape section.

#### Test Data Comparison

Representative test data is plotted with corresponding analysis in Figures 3.3-8 to 3.3-10.

From the test #2 plots, it can be seen that the back surface analyses and test data temperature histories have the same shape, and model and test temperature rises are seen to agree within 20%.

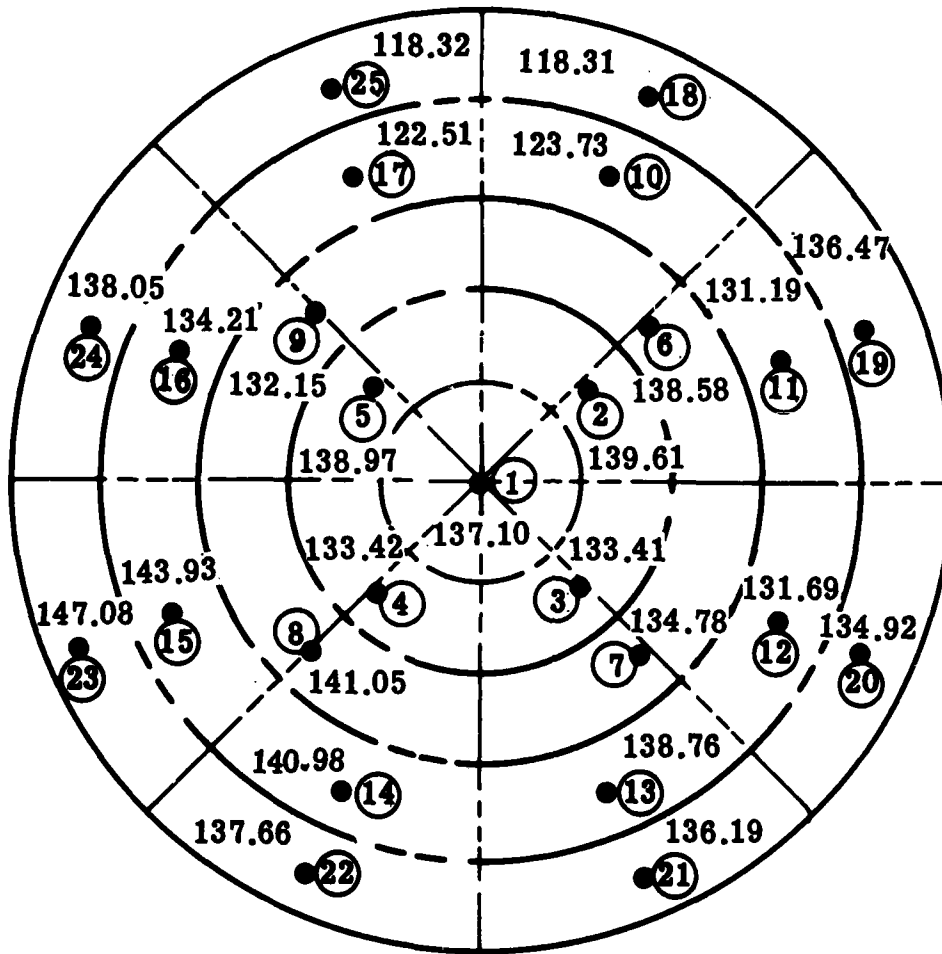
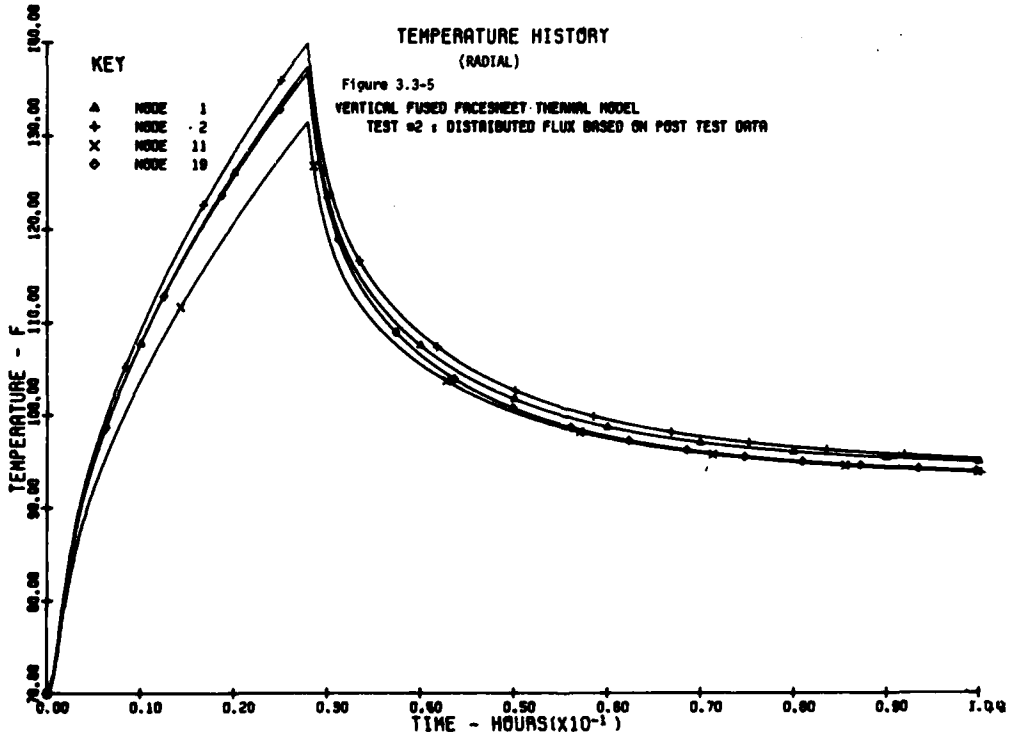
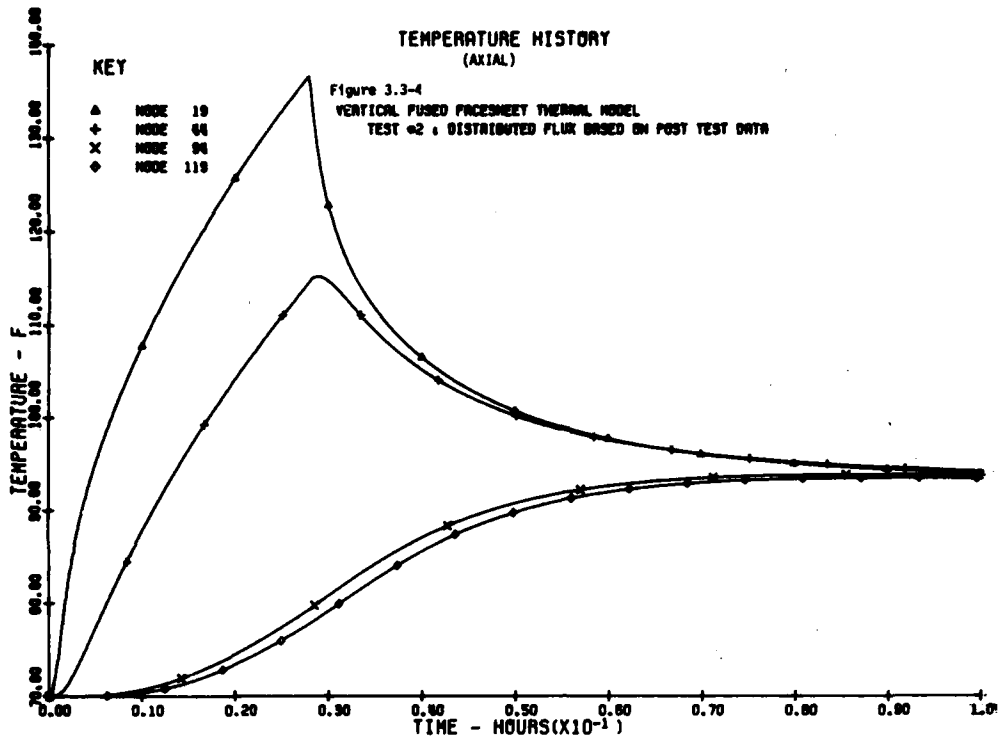
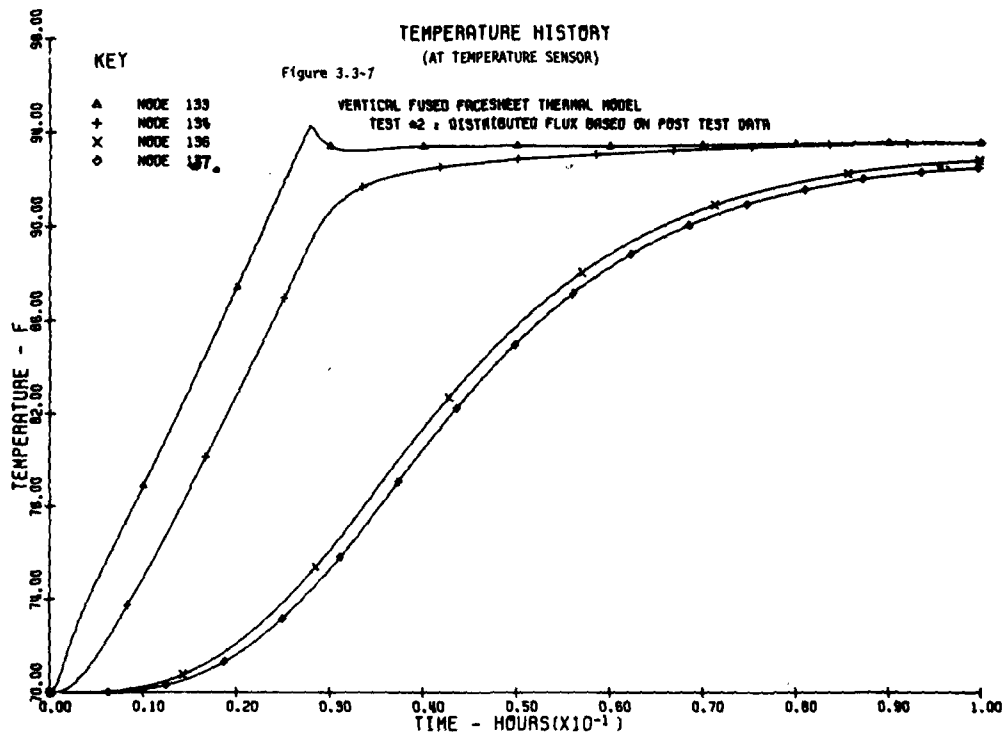
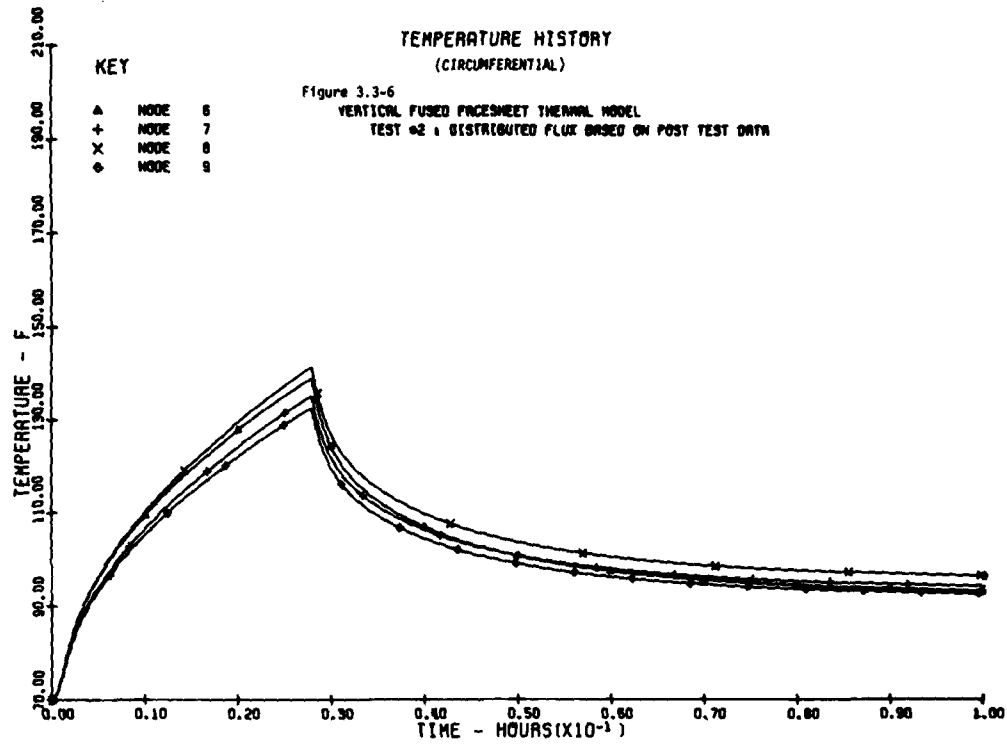


Figure 3.3-2 Temperature Distribution





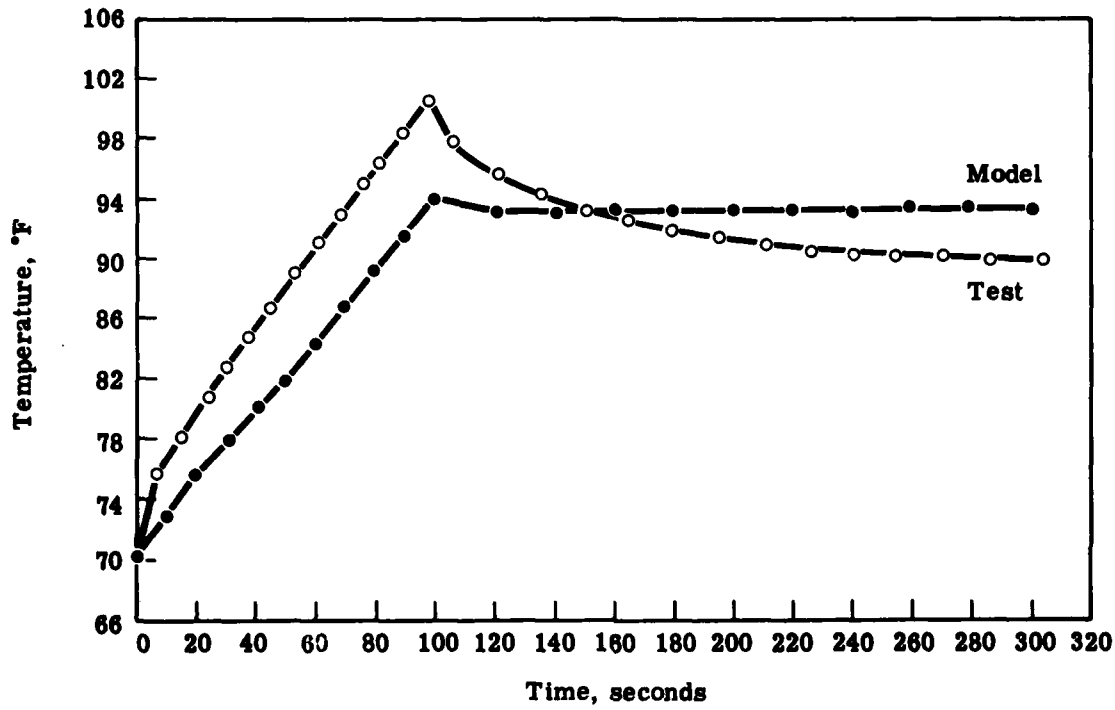


Figure 3.3-8 Temperature History for Test No. 2, 1-Meter Vertically Fused Facesheet, Hole—Front

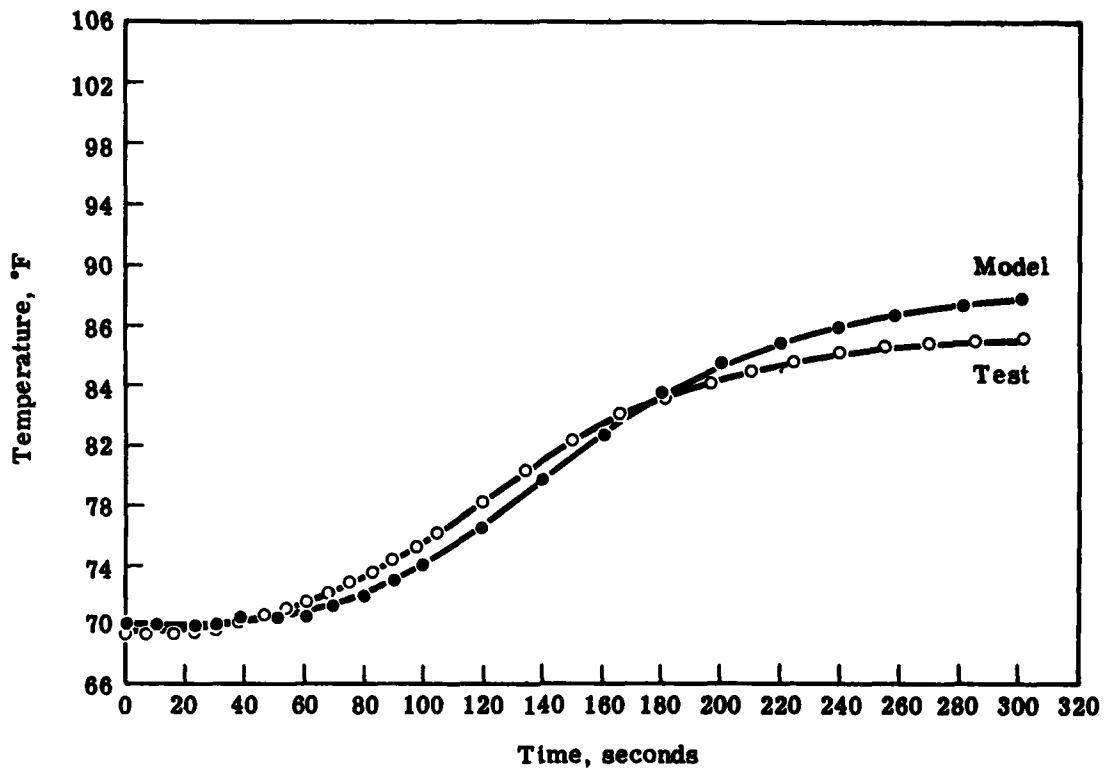


Figure 3.3-9 Temperature History for Test No. 2, 1-Meter Vertically Fused Facesheet, Hole-Back

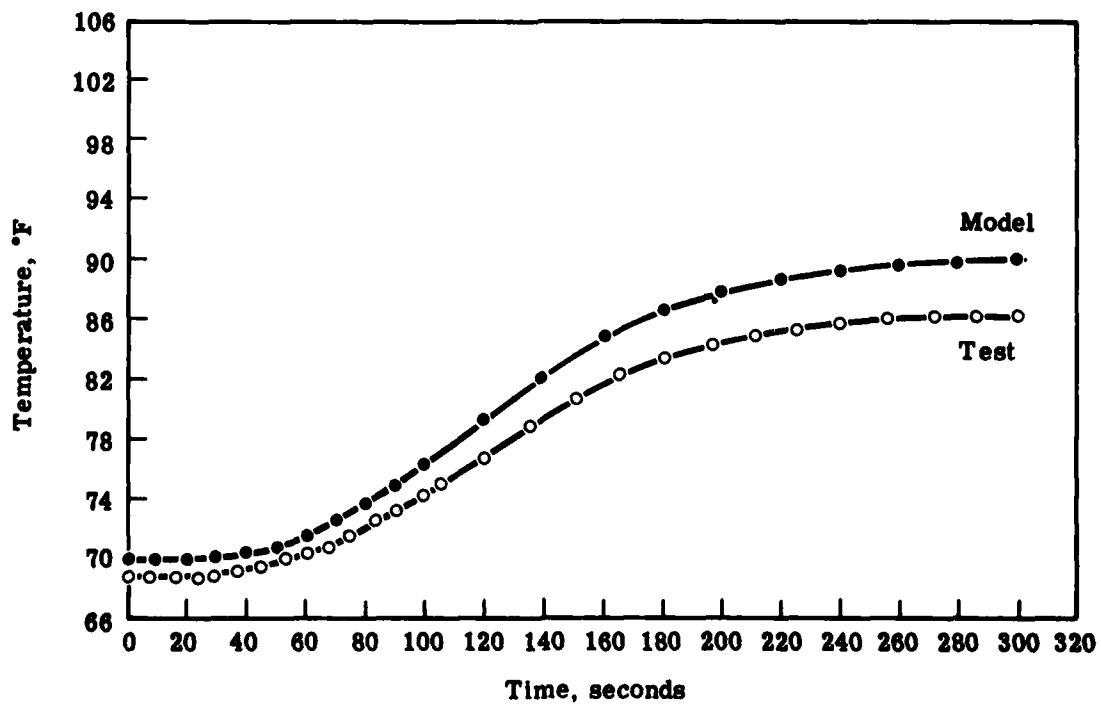


Figure 3.3-10 Temperature History for Test No. 2, 1-Meter Vertically Fused Facesheet, Centerline 7 Inches From Top-Back

The single front surface thermocouple reading differs with analysis by as much as 6°F in Test #2. This may be due to the uncertainty of the absorptance properties of the aluminum tape.

The test data of the cooling of the front surface temperature sensor is unlike that predicted in the model, test data indicates that the front surface thermocouple cools similarly to the untaped mirror, not very slowly as the aluminum tape section as the model did. This may be because the actual thermocouple was in a different thermal environment than the model's simplification. It was at the surface, not inside the top layer of the glass, therefore it did not interact as strongly with the neighboring mirror as was depicted in the model. And the high conductivity of the aluminum tape was not represented in the model, which could account for some discrepancy.

All previous conclusions indicate that the thermal model corresponds well with the actual test, as it does with most of the test data within experimental uncertainty and analytical assumption, therefore the model predictions are believed to be an accurate thermal description of the test.

### 3.3.2 Structural Analysis

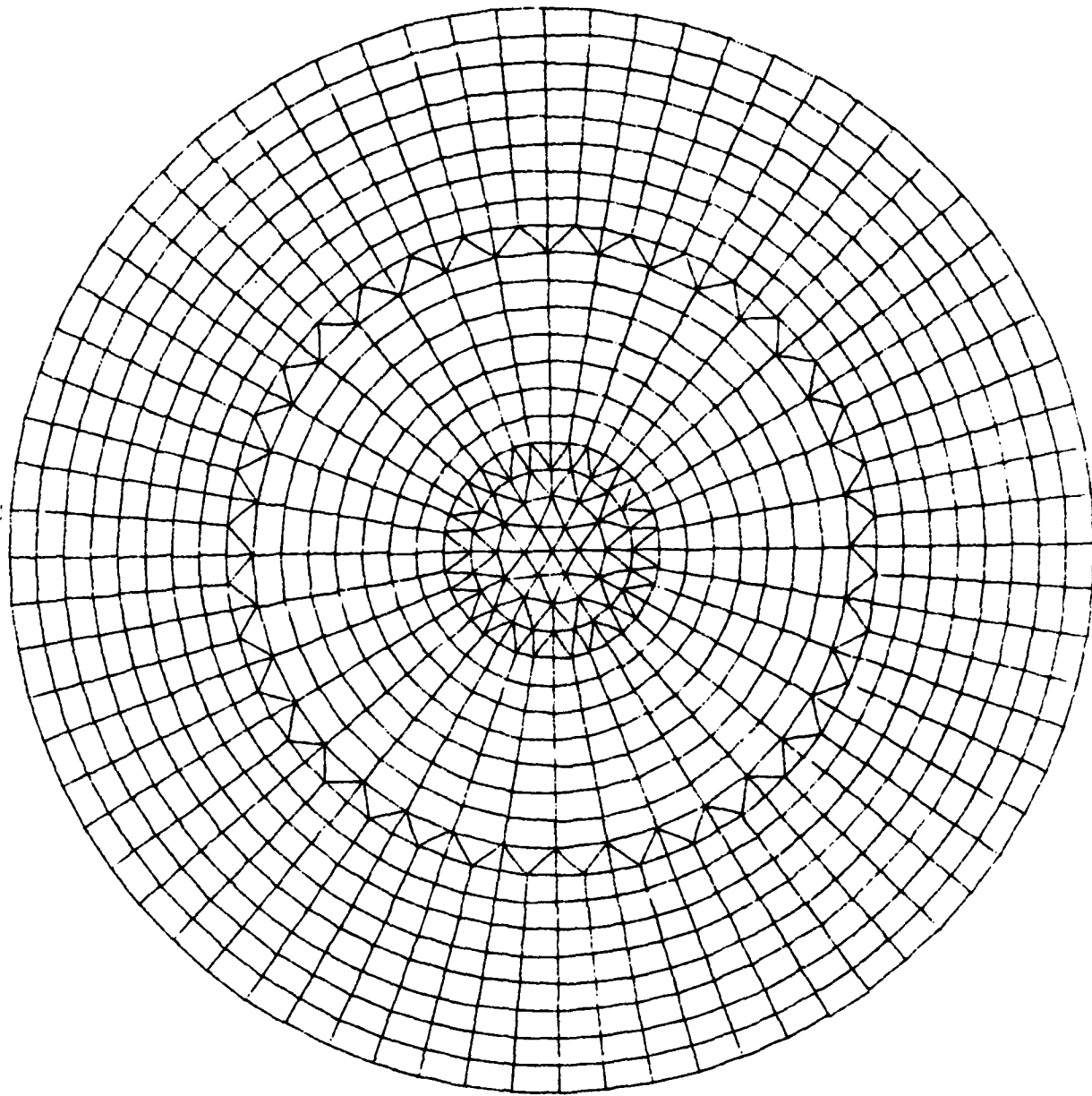
#### 3.3.2.1 Math Model Description

Since the mirror facesheet exhibits quite variable and quite low coefficients of thermal expansion, it was necessary to map such values and variations one for one on our structural model to obtain an accurate solution under the thermal flux loading. This is done on the detailed NASTRAN model shown in Figure 3.3-11. The grid network consists of 979 node points, connected by 1056 finite elements. Element thermal strain data is mapped on each of these elements at five points through the thickness in order to properly account for the effective integrated strain gradient which, under flux loading, is non-linear. Thus, the model contains over 5000 temperature inputs for each duration time considered, at 20, 40, 60, 80, and 100 seconds into the exposure.

In order to obtain the analytical prediction of wavefront aberrations, the manufacturer supplied coefficients of thermal expansion for each segment comprising the finished facesheet were mapped onto the structural model. This was accomplished via a specially written computer preprocessor which accounts for the profiles of the selective boules in which the segments were taken. The program then was utilized to map the thermal profile from the TAS thermal model and compute the effective thermal strain product ( $\alpha\Delta T$ ) at each element at five points through its thickness. The output from this preprocessor was formulated to directly input to the NASTRAN model as a set of temperature cards. Finally, the deformed shapes obtained from the model were analyzed through the Itek optics post processor routine to determine the components of the wavefront error (focus, astigmatism, coma, etc.).

#### 3.3.2.2 Mirror Mount Analysis

Since the coefficient of thermal expansion of ULE glass is so low, it was important to understand the amount of anticipated gravitational sag of the mirror in order to be able to interferometrically remove it. Since the



(Plan View)

Figure 3.3-11 NASTRAN Structural Model

one meter mirror facesheet thickness is only twenty millimeters, representative of larger diameter irradiated designs, a high D/t ratio of 50:1 results. Such a design is most sensitive to gravity loading. If tested with surface looking up on a three point kinematic mount scheme, a surface error of nearly 100 waves peak would result, predominantly tricorn, making measurement of the anticipated thermal errors impossible. If the mirror were tested on edge, a significant error of up to 30 waves peak could still result. If this error could be reduced somewhat and shown to be of low order spatial components, however, optical removal of such error could be made. Physical removal by polishing in the error was deemed costly and difficult.

A study was thus undertaken to choose the best mount scheme to help negate the gravity error. Utilizing the NASTRAN finite element model of the facesheet, several cases were investigated. These included three point mounting at varying radii, single and double V-block mounts, and sling mounting at various angles of wrap. A summary of some of these cases is shown in Figure 3.3-12. As noted, while large errors result, the sling mount errors are predominantly cylindrical. For the 120° wrap in particular, over 90% residual is removed after cylindrical fit, therefore this scheme was chosen for the thermal tests. Gravitational residuals remaining could then be subtracted from the thermally induced errors. Analytical contour of the sling gravity effect is shown in Figure 3.3-13 before cylinder removal.

### 3.3.3 Analytical Results - Performance Prediction

As described earlier, results from the thermal math model were imposed upon the detailed structural math model for the two analyzed and tested flux level conditions. Because no closed form solution utilizing the variations of CTE and thermal non-uniformities could be obtained, the NASTRAN model was thoroughly scrutinized to ascertain its validity. The results of a uniform strain gradient were compared to the theoretical solution.

In fact, it is easily shown that a kinematically mounted circular flat plate subjected to a linear thermal gradient through its thickness results in a spherical deformation well approximated by the relation:

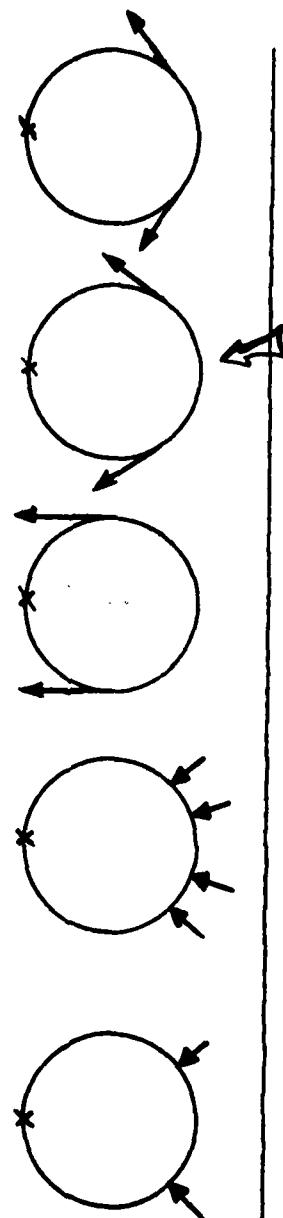
$$y = \frac{\alpha \Delta T D^2}{8t} \quad (1)$$

where  $\alpha$  is the material coefficient of thermal expansion,  $\Delta T$  the difference in temperature between the top and bottom surfaces of the plate, D the plate diameter and t the plate thickness.

For circular kinematic mirrors which have a finite radius of curvature, however, the mirror shell under the described gradient no longer remains in the stress free state afforded by the flat condition, so that equation (1) no longer applies.

To illustrate what happens to the residual error before and after focus correction, the detailed NASTRAN model of the 40 inch diameter mirror was made, with the mirror thickness varied accordingly. The model was initially run as a flat plate, and the results found to agree with the theoretical solution to within one-half of one percent. A radius of curvature of 175 inches was then included to represent our curved optic.

FIT RESIDUAL	3-POINT	5-POINT	SLING MOUNT		
			120° WRAP	180° WRAP	90° WRAP
LINEAR	4.7	1.7	4.8	2.6	5.8
FOCUS	4.2	1.1	4.6	2.1	5.7
ASTIGMATISM	2.6	0.95	0.40	0.57	0.60
COMA	2.5	0.87	0.15	0.43	0.46



All values in waves surface, RMS,  $\lambda$ -063 $\mu$ m each succeeding fit includes all aberrations above

● 120° SLING MOUNT CHOSEN FOR EASE OF CYLINDER REMOVAL (ASTIGMATIC CORRECTION)

Figure 3.3-12 VERTICAL TEST EDGEWISE GRAVITY SAG PREDICTION - MIRROR MOUNT OPTIMIZATION



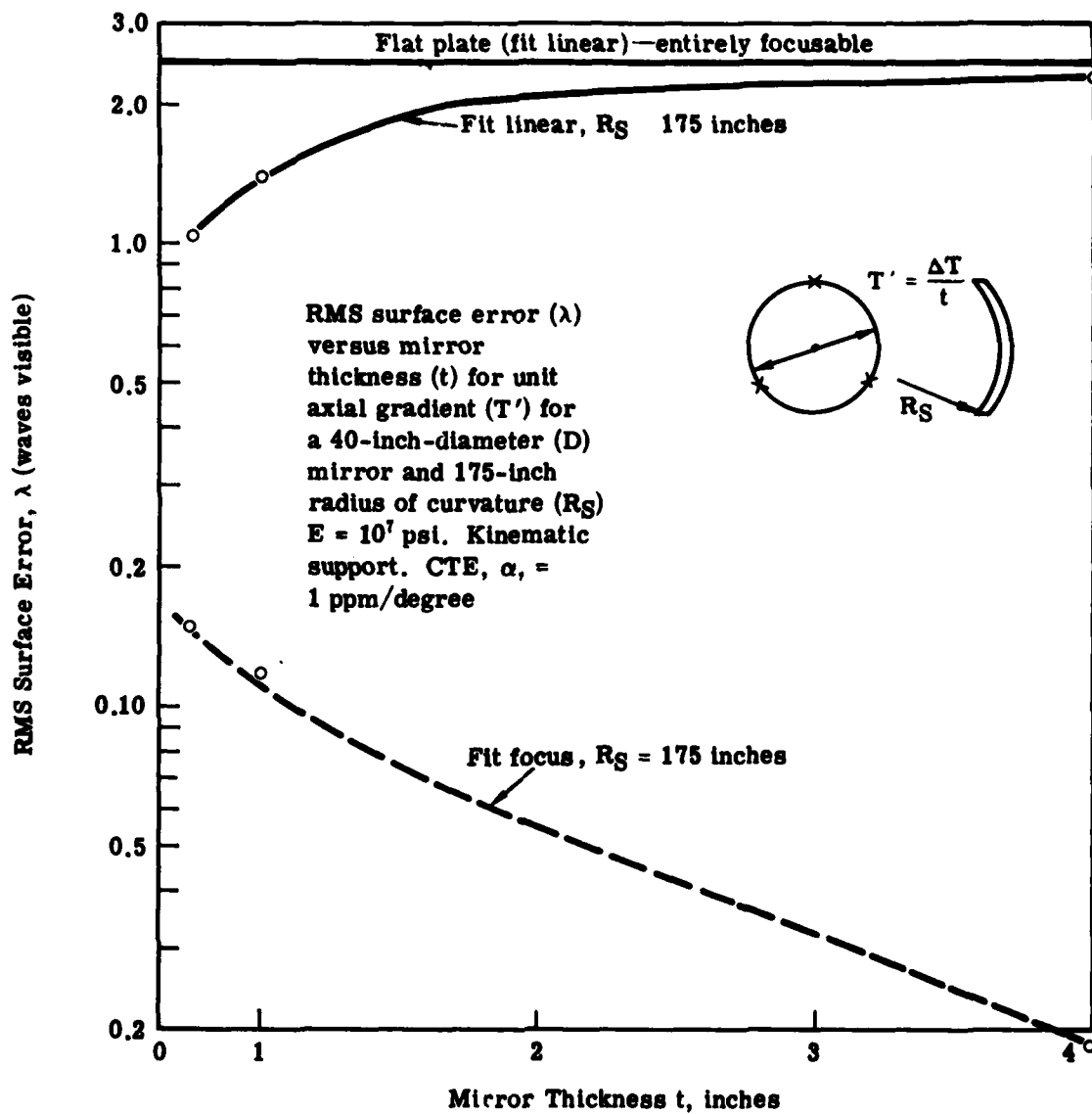


Figure 3.3-14 RMS Surface Error ( $\lambda$ ) Versus Mirror Thickness ( $t$ )

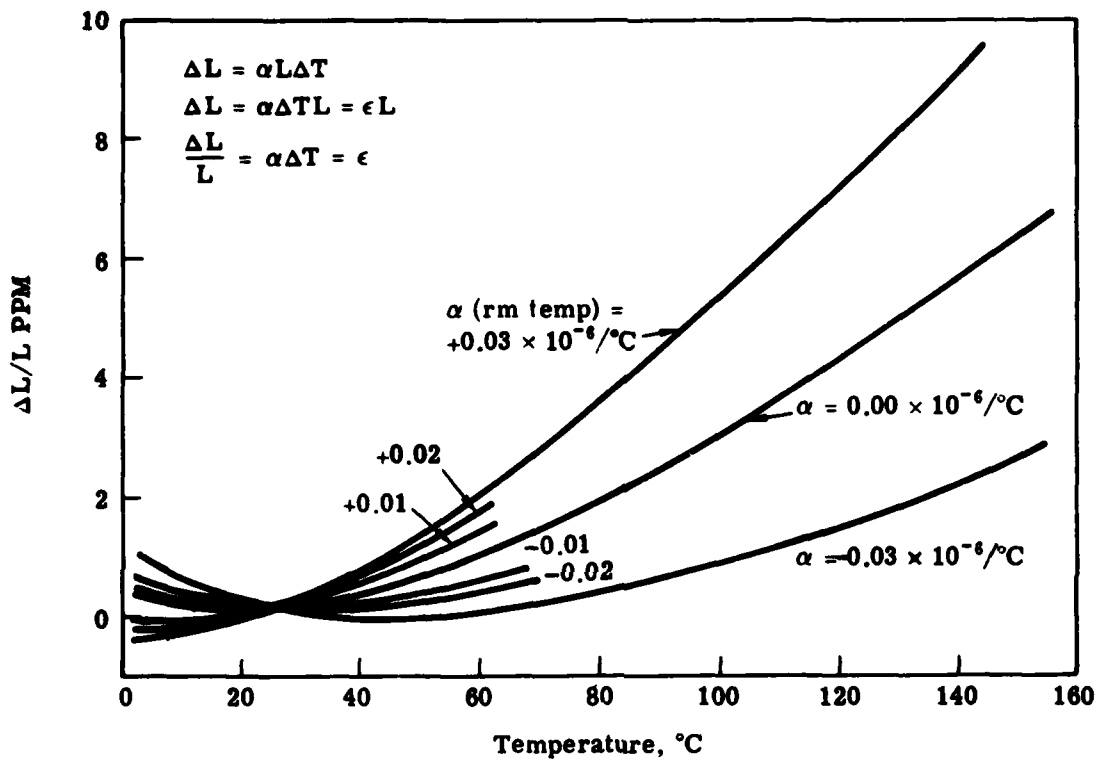
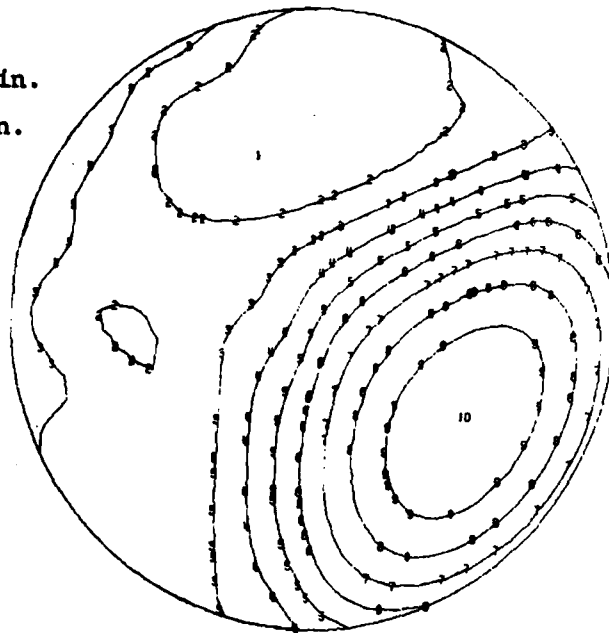


Figure 3.3-15 Thermal Expansion for Code 7971 ULE (Corning G.W. Measured Data)

Contour 1 =  $-2.4\mu\text{-in.}$

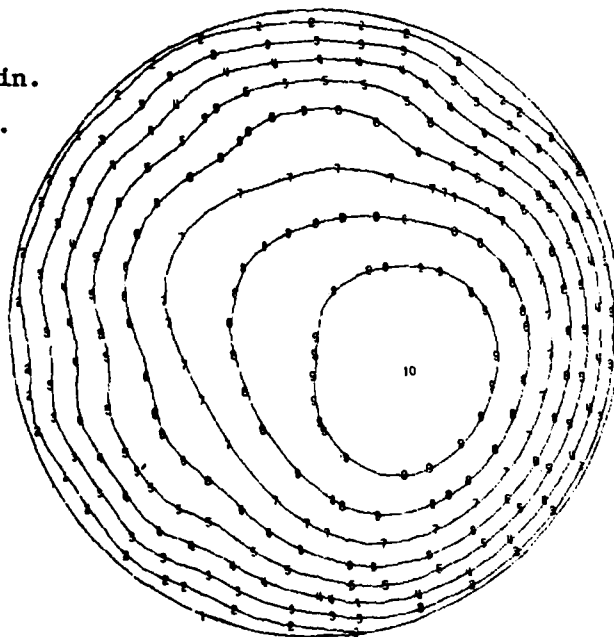
Contour 10 =  $+5.0\mu\text{-in.}$



20 seconds of flux

Contour 1 =  $-2.4\mu\text{-in.}$

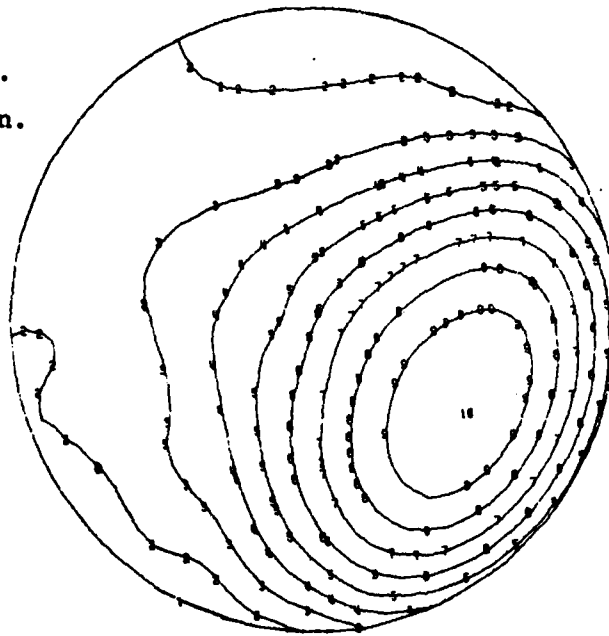
Contour 10 =  $+31\mu\text{-in.}$



100 seconds of flux

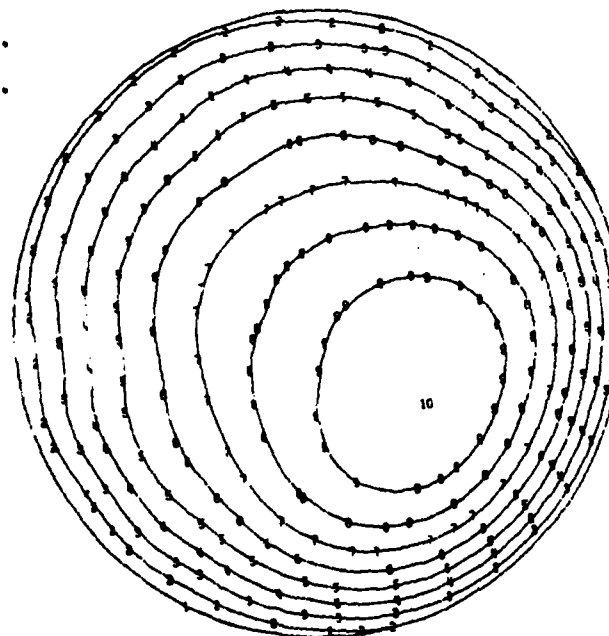
Figure 3.3-16 NASTRAN Contours of Distortion for Low Flux Case  
(z Displacements Shown)

Contour 1 =  $-2.8\mu\text{-in.}$   
Contour 10 =  $14.5\mu\text{-in.}$



20 seconds of flux

Contour 1 =  $-6.6\mu\text{-in.}$   
Contour 10 =  $+88.7\mu\text{-in.}$



100 seconds of flux

Figure 3.3-17 NASTRAN Contours of Distortion for High Flux Case  
(Z Displacements Shown)

Utilizing a constant unit gradient through the mirror thickness, the resulting displacements from the math model were then input to the Itek OPTICS package to determine residual error both before and after focus. The results are shown in Figure 3.3-14. As evidenced by the curves, the departure from the flat plate error is most pronounced as the diameter to thickness ratio increases. For a D/t of 50:1, as is our design, the error is about 2.5 times less than the flat plate without correction. After focus, however, about 15 percent residual still remains, whereas the flat plate error is entirely focusable. For a D/t of 10:1, the uncorrected error is very close to that of the flat plate, while the residual error remaining after focus is less than 1 percent.

We conclude that the shell effect reduces the residual error before a focus fit, under a thermal axial gradient. After focus, the residual error may be significant. This phenomenon is validated by shell theory.

Satisfied with the model performance, the test levels were superimposed on the model in conjunction with the measured CTE data across the facesheet as illustrated in Figure 3.1-2. The Corning measured values, however, are valid only near room temperature. As temperature increases, the thermal strain behavior of ULE glass is non-linear; that is, the coefficient of thermal expansion is not a constant. This is evident by the thermal expansion strain curves for ULE glass shown in Figure 3.3-15. Thus, the facesheet room temperature data were imposed upon these curves to obtain the true variation of strain over the entire region of the flux level loading. For ease in programming to the preprocessor which would generate the temperature cards necessary for the NASTRAN program, a table look up interpolation chart was prepared to generate an effective coefficient of thermal expansion at any temperature input as predicted by the thermal analysis. The effective coefficient of expansion is defined as the total strain to the temperature level of interest divided by the temperature change. These values are shown in the chart of Table 3.3-5. It is noted that at the higher flux temperature levels, effective CTE is increased markedly from the room temperature level. Detailed results of the low and high flux cases are summarized in the appendix. Shown are the residual errors for no fit and various fits, both rms and peak to peak, at selected intervals of irradiation duration. Also shown are the predicted amounts of power, cylinder, coma, and other aberrations. Shown in the plots of Figures 3.3-16 and 3.3-17 are the NASTRAN contours of distortion at 20 and 100 seconds for both tests.

### 3.4 Test Evaluation

#### 3.4.1 Test Summary

The irradiation test evaluation for the one-meter facesheet was conducted inside the Dynamic Resolution Test (DRT) chamber Itek in a vacuum sufficient to eliminate air turbulence for good interference mic photography. A pictorial of the test set-up is shown in Figure 3.4-1. A photograph of the test set-up at the rear of the chamber is shown in Figure 3.4-2. A photograph inside the chamber viewing the back of the lamp simulator and the front of the

Table 3.3-5 CTE (effective vs. Temperature)

(68°F) 20°C (Measured values)	(104°F) 20-40°C	(140°F) 20-60°C	<u>Difference</u> (max-RT)
$-.018 \times 10^{-6}$	$-.010 \times 10^{-6}$	$+.007 \times 10^{-6}$	$.025 \times 10^{-6}/$
-.017	-.008	+.008	.025
-.016	-.004	+.009	.025
-.014	+.000	+.010	.024
-.013	+.005	+.013	.026
-.011	+.010	+.018	.029
-.009	+.010	+.019	.028
-.008	+.011	+.020	.028
-.007	+.012	+.021	.028
-.005	+.012	+.022	.027
-.002	+.014	+.025	.027
-.001	+.015	+.028	.029
+.004	+.017	+.029	.025
+.006	+.018	+.030	.024
+.007	+.020	+.031	.024
+.008	+.022	+.032	.024
+.009	+.024	+.034	.025
+.010	+.025	+.035	.025
+.011	+.026	+.038	.027
+.012	+.027	+.040	.028

mounted facesheet is shown in Figure 3.4-3. The details of the testing will be discussed below.

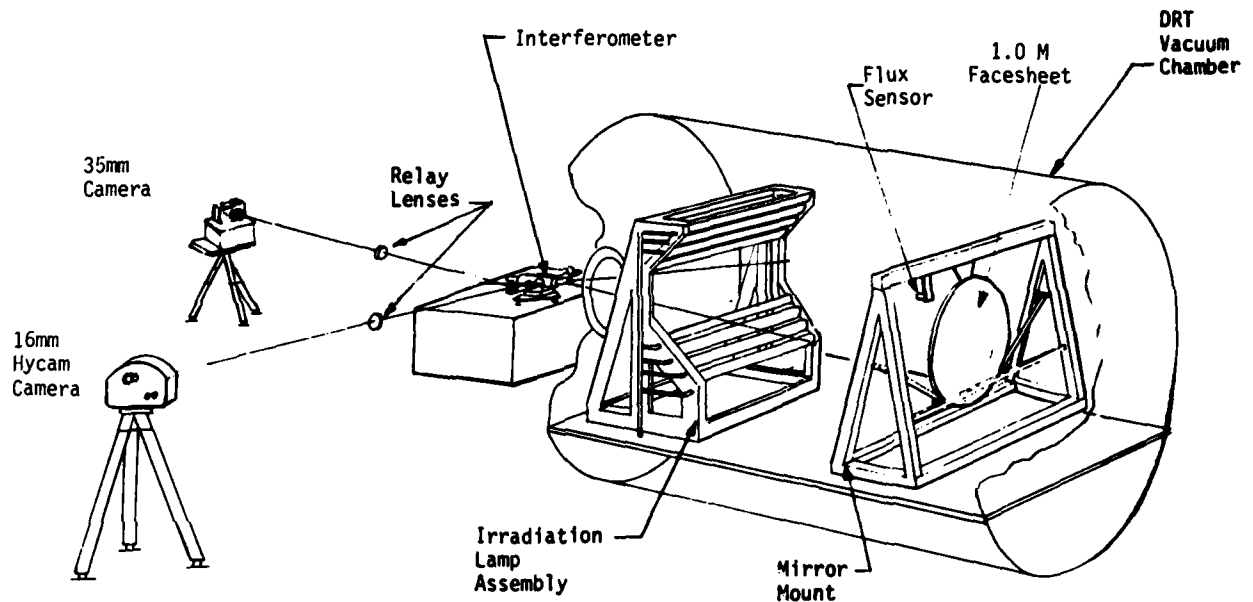


Figure 3.4-1 IRRADIATION TEST SET-UP

The primary objective of the test was to interferometrically measure and record the optical surface figure changes of the one-meter facesheet during 100 second periods of high thermal irradiation. Temperature data was also recorded to assist in correlating analytical temperature predictions. Two mirror tests were conducted for two flux load levels of 100 seconds each for two mirror orientations. Test data appeared to be of good quality for evaluations, including 32,000 frames of interferograms.

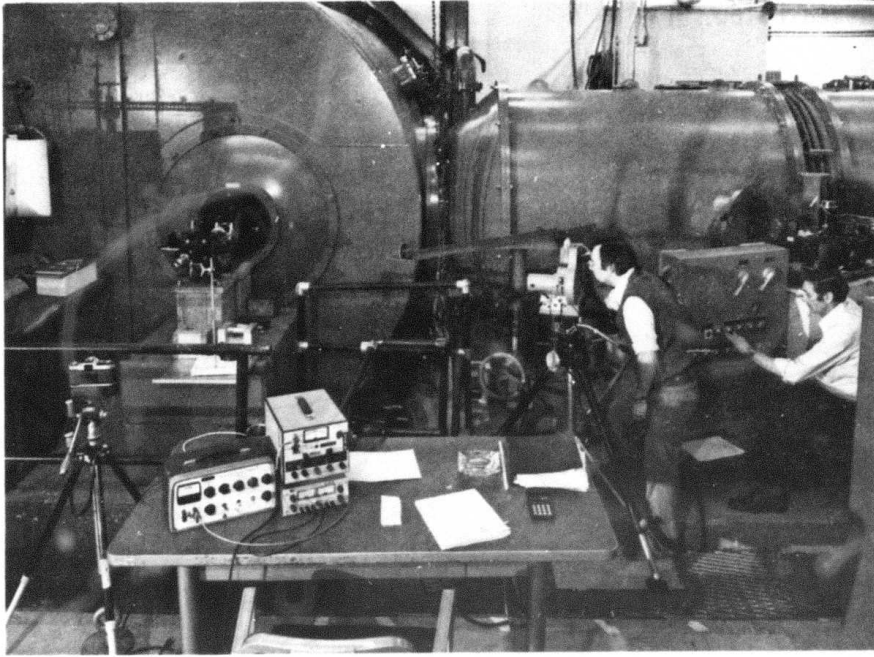


Figure 3.4-2 Test Setup Outside the DRT Chamber

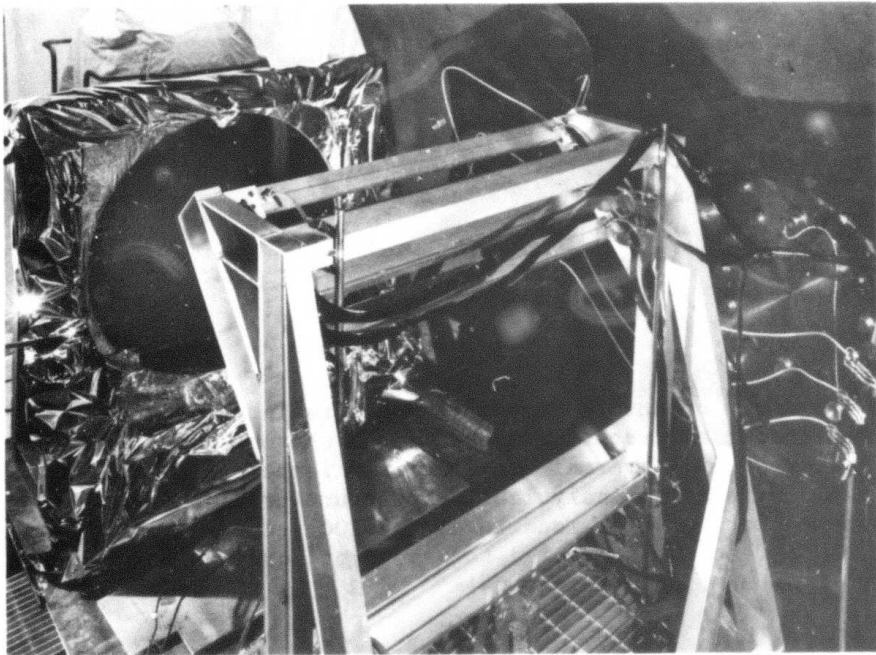


Figure 3.4-3 1-Meter Facesheet and Lamp Simulator Mounted in DRT chamber

### 3.4.2 Test Method

Irradiation - High intensity, thermal flux loading for the mirror was provided by tungsten-quartz infrared lamps used in conjunction with a high absorptance coating on the mirror. A black chrome coating was utilized to provide the high absorptance for the lamp output and yet provide sufficient reflectance for good interferometric measurements.

In order to characterize the coating absorptance ( $\alpha$ ), it is necessary to measure  $\alpha$  over the spectral output of the lamps. The  $\alpha$  was determined from the relation:

$$\alpha = 1.0 - \text{reflectance} - \text{transmission}$$

where reflectance and transmission were measured over the wavelength range of 0.4 to 5.0 microns from a witness sample taken when the facesheet was coated. The spectral radiance of the lamps for this test and the coating absorptance as a function of wavelength are shown in Figure 3.4-4. The integrated average  $\alpha$  over the range of output of the lamps was found to be 0.690, and takes into account a small amount (about 4%) of measured transmission through the black chrome. The spectral radiance was calculated from 0.4 to 4.3 microns and was adjusted for coating absorption and transmission, and quartz transmission. The irradiance peaks at about 2.3 microns and drops to zero at 4.3 microns because of low transmission of quartz glass beyond that point.

Optics - The mirror's figure during irradiation tests was measured in a center of curvature set-up using a Twyman-Green interferometer, at 0.633 $\mu$  wavelength. Data was recorded by imaging the mirror aperture simultaneously on a 35mm camera and a 16mm cine camera during the 100 second irradiation period. Exposures were taken on the 35mm camera before the lamps were turned on, at 10 second intervals during irradiation and after the lamps were turned off. The 16mm cine camera was operated at 175 frames per second for test #1 and 160 frames per second for test #2.

In its vertical sling mount, the fused facesheet exhibits a significant gravity sag, a total of about 5 waves surface RMS (at 0.633 $\mu$ m). Also, the final figure of the facesheet has about 2 waves peak surface error of astigmatism. In order to reduce these baseline errors to a manageable level, an astigmatism corrector was used. This corrector consists of a tilted pair of plane-parallel glass plates positioned in front of the interferometer. The plates were adjusted to induce a constant amount of astigmatism in the optical path to compensate for mirror and mount induced astigmatism. Baseline interferograms showed about 0.5 waves RMS, surface errors after adjustments to the corrector plates.

Data was recorded on two cameras to allow figure reduction at discrete intervals (using the 35mm film), and to allow a particular fringe to be followed throughout the test (using the cine camera). Following a particular fringe enables the axial displacement of the mirror surface to be measured. Knowing this axial movement and knowing the total fringe focus change in the interferograms, the actual radius change in the test mirror can be calculated.

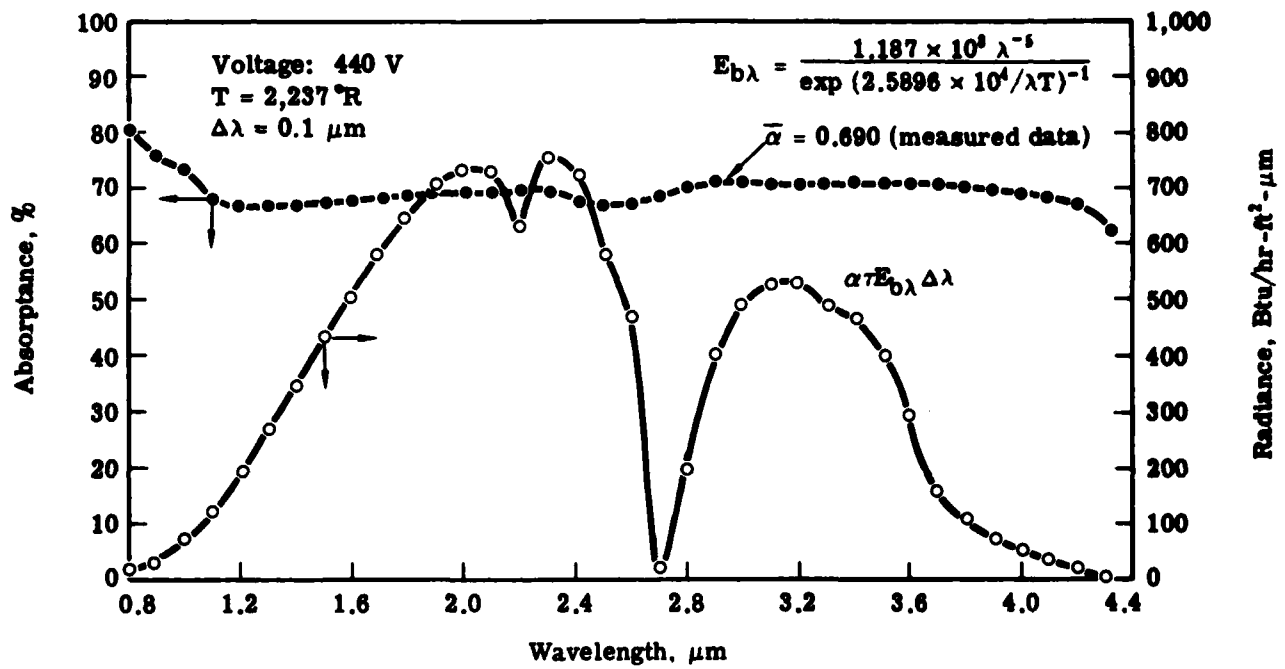


Figure 3.4-4 Spectral Radiance and Absorptance for Black Chrome Coating Irradiated by Tumpton-Argon Quartz Lamps

### 3.5 Test Equipment and Instrumentation

The equipment and instrumentation used for this test is listed in Table 3.5-1. All instruments were calibrated for the test period according to standard Itek policy.

Temperature data was recorded using 28 gage copper-constantan, Type T, thermocouples. Thermocouple calibration data is shown in Table 3.5-2. All thermocouples were measured with the Fluke recorder used for the test as a system calibration and compared with a laboratory mercury thermometer, No. F634G. Thermocouple locations are shown in Figure 3.5-1.

Dynamic Resolution Test (DRT) Chamber - The DRT is a large, cylindrical, walk-in vacuum chamber which is equipped with a full-diameter access door, electrical power, instrumentation, and liquid pass-through port capability. A 19-inch diameter by 1.25-inch thick optical window is mounted to the rear wall for interferometric evaluations. A substantial interferometer mounting block is located exterior to the chamber window position. The chamber and mounting block are attached to a common vibration-isolated platform. Each irradiation response test was conducted at a pressure level of 6 Torr.

Irradiation Calibration Frame - The calibration frame was assembled to allow accurate horizontal and vertical coordinate positioning of a heat flux transducer. This provides a means to monitor the average flux density at each reference point for calibrating the irradiation uniformity of the simulator lamp assemblies. Each coordinate position was spaced at various intervals from the operational axis of the simulator assembly. A Medtherm, Type 64-05-20T flux transducer, with a range of 0 to 56.8 kw/m<sup>2</sup> and a signal output of 0 to 10mv, was employed for the uniformity adjustments. A post-test flux survey is shown in Table 3.3-3.

### 3.6 Correlation of Test and Analytical Results

The analytical results of the thermally induced error discussed earlier are now compared to the measured data. These comparisons are shown graphically for both tests in this section. In Figure 3.6-1, the measured results of the aberration terms are shown as a function of exposure time for the low flux of test 1. Given are the amount of measured power, cylinder, and coma in surface waves, peak, visible. Shown also are the angles of aberration, defined as the first high, or positive, peak along the edge, looking at the concave surface. The power term is negative, that is, such that the mirror bends convex, or into a more shallow sphere. Figure 3.6-2 shows the same aberrations as measured during the high flux of test #2. Table 3.6-1 is a summary listing of these aberrations compared side by side to the analytically predicted values at 100 seconds for both tests. As evidenced, there is an excellent correlation in power term in both size and magnitude, and a good correlation in prediction of comatic angle (angle variations of 180° in coma mean no correlation, i.e., opposite sign, while 0° difference is perfect correlation within anticipated test errors). There is, however, a rather poor correlation in measured versus predicted cylinder as well as angle of cylinder.

To understand the correlations, the chart of Table 3.6-2 was prepared to show side by side the residuals remaining after selected fits for all dura-

Table 3.5-1 VERTICALLY FUSED FACESHEET TEST EQUIPMENT LIST

<u>ITEM</u>	<u>DESCRIPTION/ACCURACY</u>	<u>DWG. PART/ID NUMBERS</u>
1. Irradiance Simulator	Aluminum mounting structure to support lamps and cooling and electrical lines.  Lamps (8 assemblies) are tungsten-argon-quartz lamps with a required water flow of 0.29gpm/reflector at 70°F or less. Each lamp powered with 440 volts for his study.	DWG#162570 & 165389  Research, Inc. Model #5193038
2. Irradiance Calibration Frame	Aluminum structure that allows the flux transducer to scan an area simulating the mirror surface	DWG#165336
3. Power Supply Controls	Provides for on/off switching of lamp groups along with internal timing cycle and water pressure safety circuit.	DWG#162492
4. Heat Flux Transducer	Range: 0 - 0.5 BTU/ft <sup>2</sup> sec (0-56.8Kw/m <sup>2</sup> ) Output Signal: 0.1 mv Cooling: 0.3gpm at 50 psig	Medtherm 64-05-20T Serial #4693
5. Differential Voltmeter	Differential Voltmeter to read millivolt signal from flux sensor	Fluke Model 873A Itek, ML-4574 Accuracy ±.01 millivolts
6. Cooling Manifold	To provide ~ 3 gpm to reflectors and .5 gpm to transducer. (requires a flexible hose for connection of the transducer to the coolant manifolds) safety interlock switch to lamp control set to approximately 20 psig.	DWG#165333
7. Mirror Mounting Assembly	Aluminum A-frame with 120° sling mount for the 1.0 meter facesheet. Features include a heat mask and mounting provisions for the flux sensor.	DWG#230243
8. Laser Unequal Path Interferometer	4m watt laser f/2.8 diverger (made at Itek) Relay Lenses to 35mm Olympus - 22 inch focal length to Hycam - 26 inch focal length 1½ inch cube beamsplitter in relay arm (to split Olympus and Hycam beams)	Mini #3 (no Itek K#) (No Itek K #) (No Itek K #)
9. 35mm Camera	Type Tri-X film Shutter speed 1/500 second	Nikon (Itek K#1202 and 1203)
10. Cine Camera	Run at 160 & 175 frames/second. Effective shutter speed 1/500 second. Type RAR 2498 film on 450 foot reels.	Redlake Hycam Claus Gelotte #MA2614
11. Thermocouples	Copper Constantan - 18 used	#28CCGT (calibrated)
12. Thermocouple Recorder	18 channels used, maximum scan rate 2½ lines per second	Fluke #220B Itek ML08442

**Table 3. 5-2 Thermocouple Calibration for Vertically Fused Face Test**

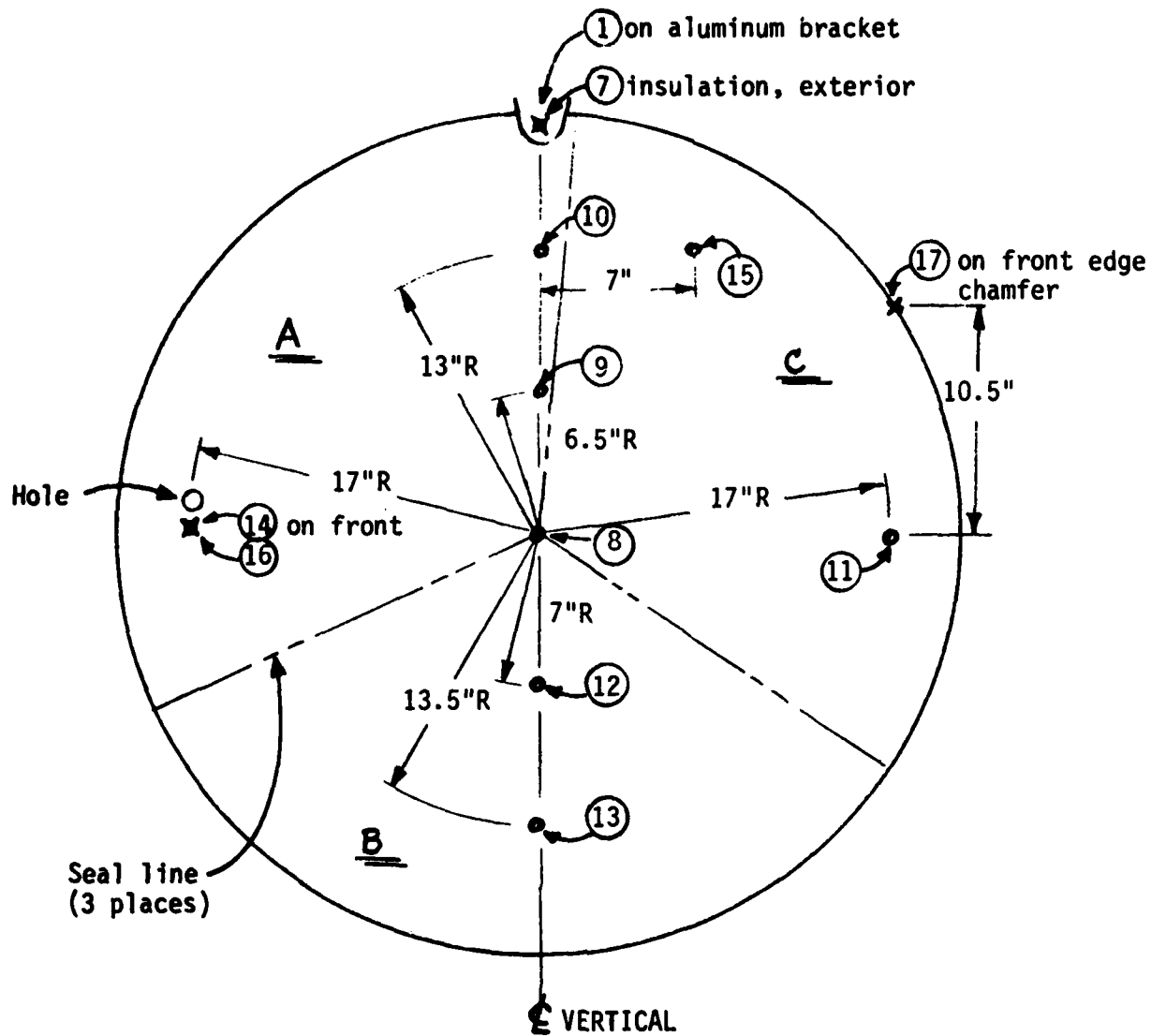
**Thermocouples:** Type T, 28 gage copper-constantan

**Recorder:** Fluke model 2200B data logger

**Comparison Standard:** Laboratory mercury thermometer, No. F634G

Data represents two sample average in room temperature water and boiling water.

Thermocouple No.	Standard, 72.9 <sup>0</sup> F		Standard, 212.0 <sup>0</sup> F	
	Temperature 0F	Correction factor, 0F	Temperature 0F	Correction factor, 0F
1	72.5	+ .4	212.3	- .3
2	72.6	.3	212.1	- .1
3	72.9	0	212.1	- .1
4	72.6	.3	211.9	+ .1
5	72.7	.2	211.7	.3
6	72.7	.2	211.8	.2
7	72.9	0	211.7	.3
8	72.7	.2	211.7	.3
9	73.0	- .1	211.6	.4
10	72.4	.5	211.4	.6
11	72.5	.4	211.4	.6
12	72.5	.4	211.5	.5
13	72.8	.1	211.6	.4
14	72.5	.4	211.5	.5
15	72.4	.5	211.4	.6
16	72.5	.5	211.3	.7
17	72.6	.3	211.5	.5



View looking at coated surface (concave side)

- facesheet: ⑧ to ⑰ on back surface unless noted otherwise
- top bracket: ① & ⑦ as noted

Other locations not shown:

- lamp housing, lamp #1: ②
- chamber air @ flux sensor: ⑥
- chamber air behind frame: ③, ④, ⑤
- chamber window, half radius: ⑱

Note: The view shown represents locations for test #1. For test #2, the mirror (and T/C locations) were rotated 180°.

Figure 3.5-1 Thermocouple Locations for Vertical Fused Facesheet Test

tions for both tests. As evidenced, there appears to be an unfavorable correlation of residual magnitude in test 1, and a more favorable one in test 2. For test 2, the residual errors are shown as a function of time graphically with the analytical results after focus and residual fits and plotted in Figure 3.6-3. Seen here is a good residual correlation for higher order fits, but a lesser one after focus fit.

While the results showed excellent correlations in power, sign, comatic angle, and higher residual error, a further effort was undertaken to understand the lack of correlation in residual amounts after the low order fits. As noted in Table 3.6-2, the residuals of test 2 after cylinder fit show a marked correlation to the predicted values. It was deemed that perhaps some mount induced loading was generating the higher than predicted cylinder error, and, to a lesser degree, the coma error.

It is recalled that the mount scheme, a 120° sling supporting the mirror on edge with three "snubber" points to react the moment imbalance, was chosen and exhibited large cylindrical gravity errors which could be removed initially in the interferometric set-up. Studies showed the mirror to be extremely sensitive to cylinder error. Cases were exercised on the NASTRAN math model to note sensitivities to cylinder error under mount loadings of one pound or one inch pound induced at the snubber and strap support locations. These cases showed a high sensitivity to mount induced cylinder error. Optical check-out tests, discussed in the appendix, were then conducted to induce, purposely, mount type errors as afforded by sling heating and sling offsets. As in the analytical evaluation, significant cylinder induced errors up to 3 waves surface were identified.

We conclude, therefore, that the test cylinder amounts measured were most likely introduced by the sensitive mount scheme. With this considered, the chart of Figure 3.6-4 was prepared, which compares test #2 power aberration, cylinder, and residual fits to those predicted. A very good correlation is realized as evidenced, when the mount cylinder error is fit.

The results of test #1 show less favorable correlations. In this case, the lower flux level, and hence lower thermal response in conjunction with the lower effective coefficient of thermal expansion, results in a signal less than one third that of the second test. Such a low signal is masked out by mount and test errors, making the correlation difficult.

### 3.6 Results Scaled to Larger Mirrors

The facesheet material and thickness for this test was purposely chosen to simulate that of large aperture irradiated systems proposed for future design studies. For such larger systems, wavefront residuals must be required held to the order of 0.02 $\mu$ m rms surface error, demanding the use of an active or multipoint support design scheme.

The purpose of this test was to show that no fusion line effects are present and that analytical correlation to test results of a fused segment design is therefore feasible. To achieve this, the segments were purposely chosen mismatched in CTE and the mount scheme not multipoint, in order to achieve a high enough signal relative to the figured piece. If resulting errors were

correlated, extrapolation to larger, active design is readily made, since the identical assumptions, analytical techniques, and finite element modeling are utilized in their performance predictions. The correlation has been discussed in Section 3.6. In both analysis and test, the fusion lines show no ill effect, in that the mirror behaves as a continuous piece, in spite of CTE step changes between segments and significant locked in residual strain. Our analyses of larger designs have utilized boule to boule variations in excess of those of the test piece, and show low residual error achieved with proper active support mount spacing. We conclude that our test results are directly relatable to large aperture, vertically fused designs on a multipoint mount arrangement.

#### 4. CONCLUSIONS AND RECOMMENDATIONS

Based on the above discussions, it is concluded that:

- 1) Fusion line effects are non-consequential to the analyses and fabrication.
- 2) Power prediction is well correlated in both magnitude and sign.
- 3) Comatic aberration angle is well correlated as it moved as predicted when the mirror was rotated 180° from test to test.
- 4) Residual error after cylinder and higher order fits is correlated within reasonable limits.
- 5) Thermal strain variation with temperature is a must for consideration.
- 6) Predicted results are readily extrapolated to larger aperture designs.
- 7) Testing of thin facesheets requires careful mount design and detailed sensitive studies to minimize mount effects.

Table 3.6-1 Analytical and Test Comparisons  
of Aberration Peaks

Test	Time	Values in Waves Surface									
		Cylinder						Coma			
		Power		Amount		Angle		Amount		Angle	
Test	Anly	Test	Anly	Test	Anly	Test	Anly	Test	Anly	Test	Anly
1	100 secs	-2.83	-1.10	1.9	.25	101°	25°	1.2	.48	271	210
2	100 secs	-3.32	-3.10	2.4	.61	82°	20°	.8	1.8	55-70°	21

Table 3.6-2 Analytical and Test Comparisons  
of Residual Errors

Test	Time (secs)	Values in Waves Surface rms							
		Fit Focus		Fit Astigmatism		Fit Astig/Coma		Fit Astig/Coma/OR4	
		Test	Anly	Test	Anly	Test	Anly	Test	Anly
1	20	.217	.051	.105	.039	.098	.016	.092	.016
	40	.455	.077	.175	.060	.136	.027	.087	.026
	60	.558	.090	.203	.071	.155	.037	.094	.032
	80	.575	.094	.229	.077	.181	.046	.100	.035
	100	.557	.081	.237	.081	.187	.057	.110	.037
2	20	.193	.101	.096	.078	.089	.032	.073	.030
	40	.317	.172	.149	.140	.142	.061	.097	.049
	60	.413	.223	.215	.190	.205	.089	.119	.061
	80	.484	.262	.234	.232	.213	.117	.127	.068
	100	.519	.294	.247	.268	.233	.145	.128	.074

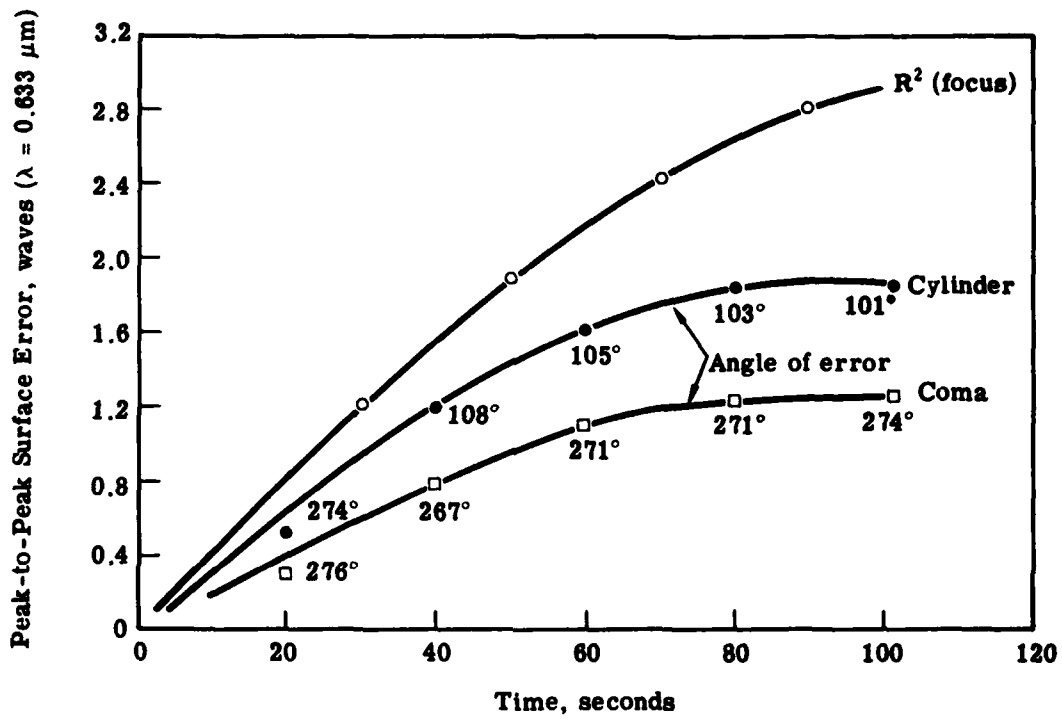


Figure 3.6-1 Measured Peak Surface Error History of Key Components of Vertically Fused Facesheet—Test No. 1

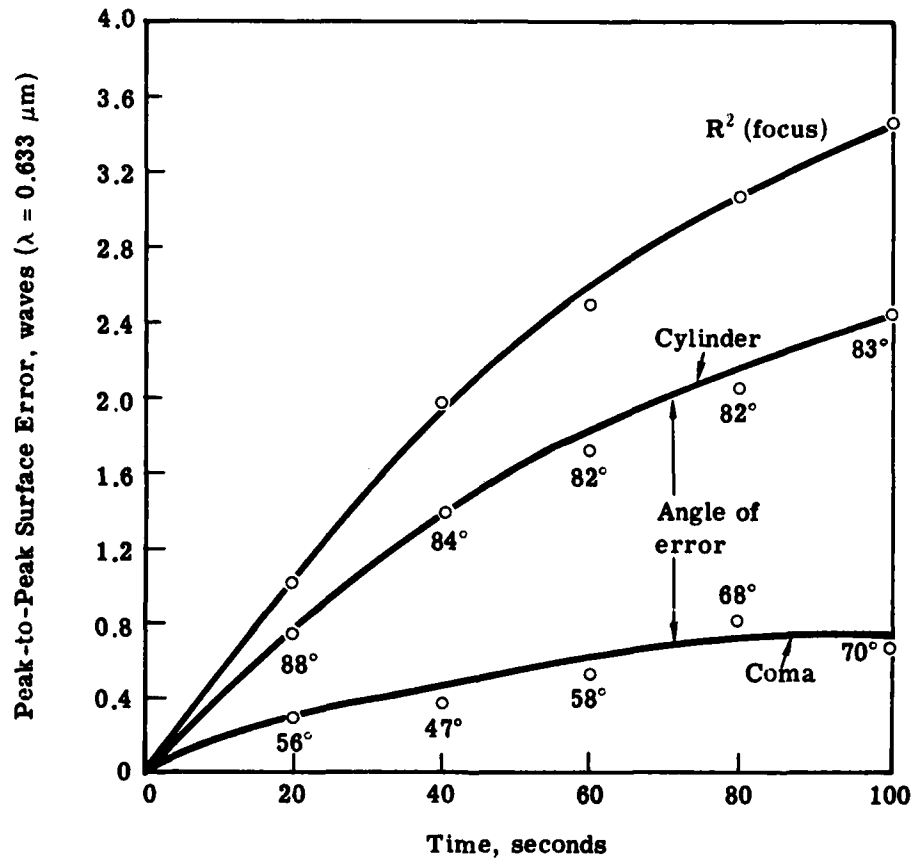


Figure 3.6-2 Measured Peak Surface Error History of Key Components of Vertically Fused Facesheet—Test No. 2

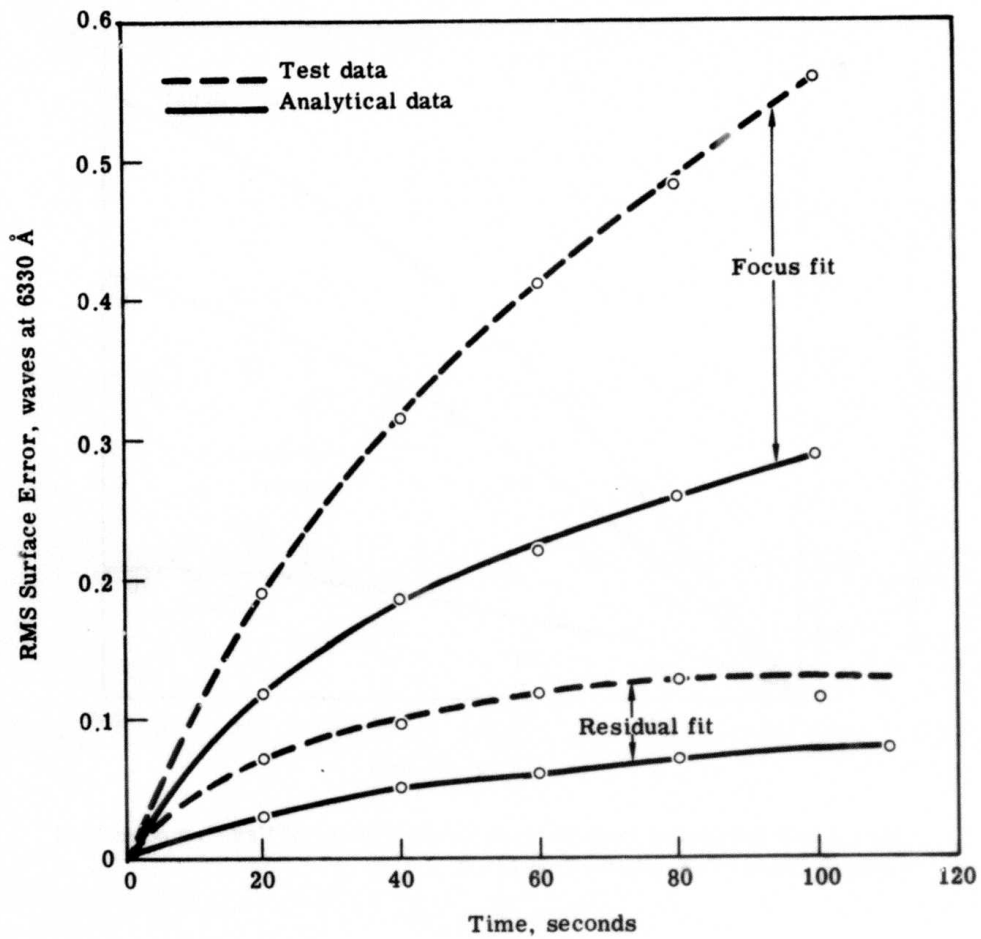


Figure 3.6-3 RMS Surface Error History for Vertically Fused Facesheet—Test No. 2, Irradiation for 100 Seconds

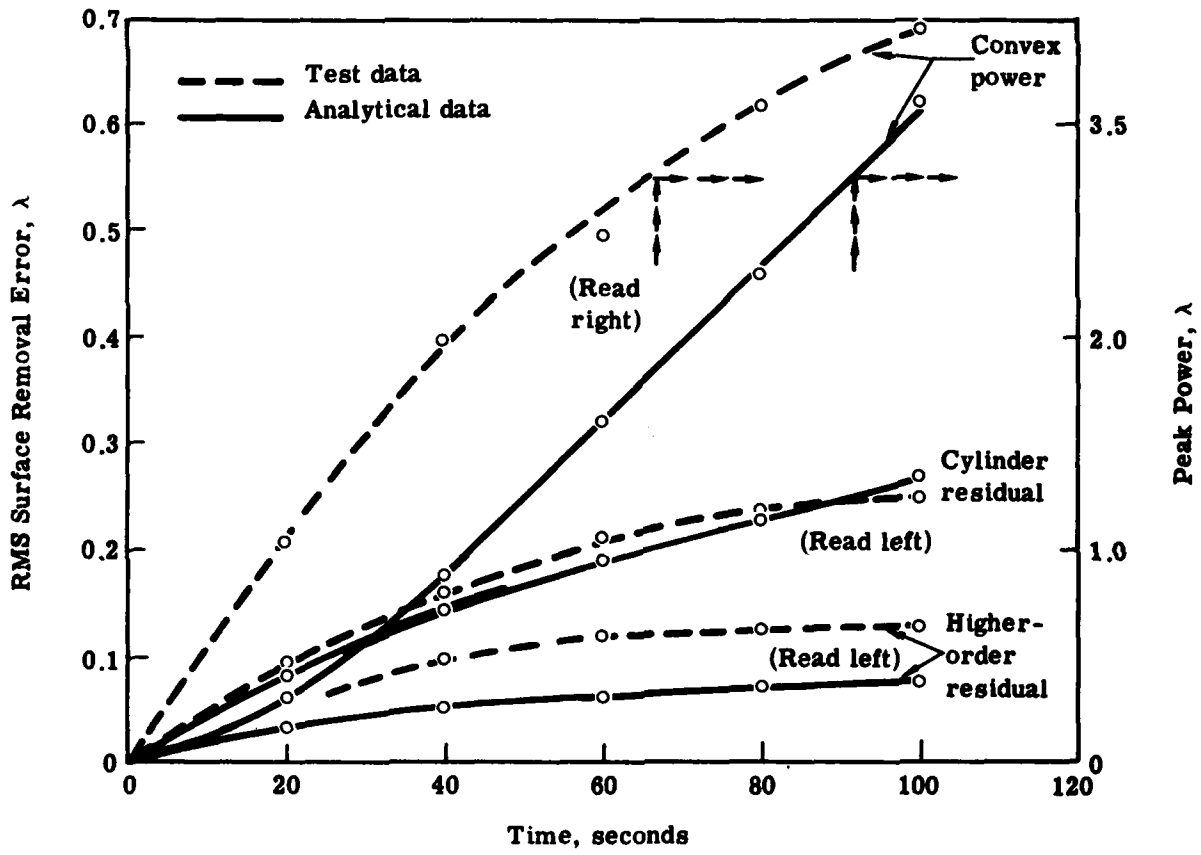


Figure 3.6-4 Test No. 2 Analytical/Test Comparisons

APPENDICES

- A. Coating Uniformity and Mount Induced Errors
- B. Analytical Results (Computer Output) for Low and High Flux Cases
- C. Analytical Temperature Histories for Test 1

APPENDIX A

Measurement of Coating Uniformity

Measurements of coating reflectivity and transmission were made across the face of the mirror to determine if an absorption variation existed during the test.

The measurements were made by observing a stable white light source with a spectro-spotmeter, reflected off and transmitted through the glass. This shows relative reflectance and transmission in the visible region. During the coating of the mirror with successive layers of chrome, measurements of reflectance and transmission were made in the visible and infrared. These in-process tests showed that the IR absorbance was tied to the absorbance value in the visible, demonstrating that an IR absorbance change is directly tied to an observed change in the visible.

The mirror was measured at six radial points; center and 4, 8, 12, 16, and 18 inches from the center. This measurement was repeated at each quadrant. These provided data both radially and transversely across the mirror.

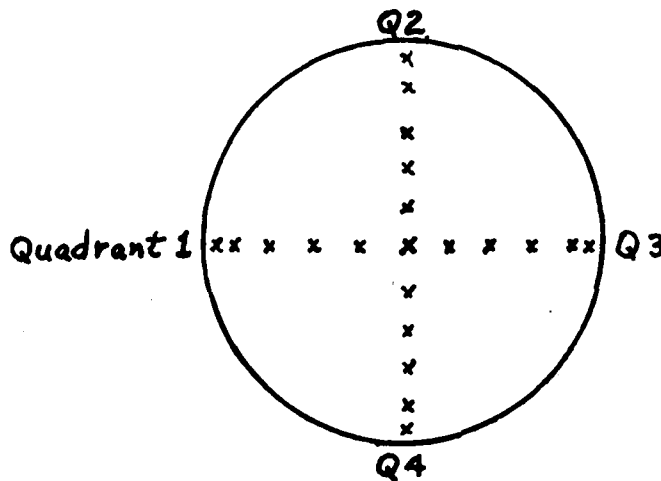


Figure 1 Absorbance Measurement Points

Test setups are demonstrated in Figure 2.

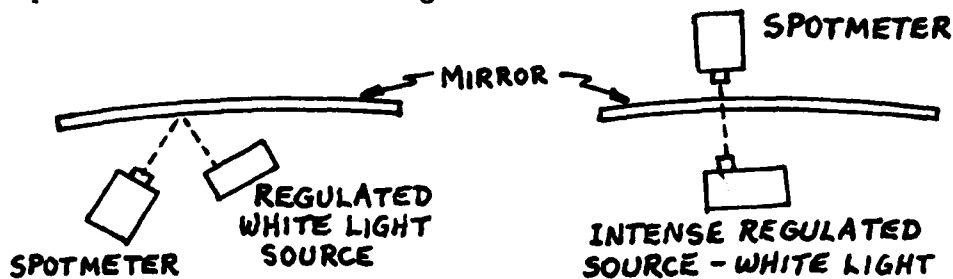


Figure 2 Transmission and Reflectance Test Setup

Reflectance results are:

<u>Radius</u>	<u>Quadrant #1</u>	<u>#2</u>	<u>#3</u>	<u>#4</u>	<u>Ave.</u>
0	17%	17.0	17.0	17.0	17%
4	17%	17.2	16.8	17.2	17%
8	16.0	17.5	16.7	17.0	16.8
12	17.5	17.7	17.7	17.8	17.7
16	18.0	18.2	18.2	18.0	18.0
18	18.0	17.8	18.0	18.0	18.0

Transmission results are:

<u>Radius</u>	<u>Quadrant #1</u>	<u>#3</u>	<u>Ave.</u>
0	.005%	.005%	.005%
4	.005%	.005%	.005%
8	.004%	.004%	.004%
12	.004%	.003%	.004%
16	.003%	.003%	.003%

Conclusion

The transmission measurements are low enough to be considered uniformly zero. Also, measured radiation leakage through the coating by pinholes was estimated (by spotmeter) to be of the same order as the coating transmission. Even doubling the transmission measurement would produce only .01% transmission-trivial compared to the reflectance.

The reflectance demonstrates a radial variation of about + 1% in absorbance. Thermal effects should be small compared to other influences.

Measurement of Mount Induced Errors

During optical alignment of the mirror for the irradiation test the mirror initially exhibited a large amount of astigmatism, not expected from analysis. This error was tracked down to excess force in the paired axial restraints (snubbers) which trapped the glass front and rear at three points. This problem was fixed, and the mirror reached a stable figure which could be reduced for a baseline for the irradiation test.

It was postulated, however, that other figure changes could have been induced by a mechanical change in the mount caused by thermal loads during the test. To quantify the mount effects on optical figure, the mirror was replaced in its mount and various changes and loads were applied while the figure was observed.

The following load simulations were applied and found to have no effect:

- 1) Tilting of the snubber bolts in their holes, imitating a lateral growth of the frame, and movement of the glass.
- 2) Moving the snubber bolts axially (screwing them in) to imitate axial growth of the snubbers.
- 3) Lengthening of the mirror strap, to simulate an elongation of the strap by heat.

Two mount changes did have noticeable effects, they are:

- 1) Rolling the mirror sideways to take a "set" away from the lowest point on the strap. The same aberrations were observed, but with opposite sign, when the movements were to left and right.
- 2) Heating the front edge of the strap to cause a temperature difference from the front to the rear of the strap. This simulates the heating from leakage of radiation around the edge of the mirror, where it abuts the insulation. The measured heat differential in the strap for this test was 5°C. The distortion causes a slight cone shape in the strap.

The aberrations induced by these two loads is shown in Figure 3.

#### Conclusion

A mount load which causes a movement of the mirror and strap as a whole has no effect on the figure. However, any movement of the mirror with respect to the strap will induce errors. Differential heating of the strap is very likely, and this variation will be used in the re-analysis. A sideways motion would be caused by an error in mounting combined with "settling" during the thermal cycle. While this is a possibility, it is not provable or predictable, and will not be considered here.

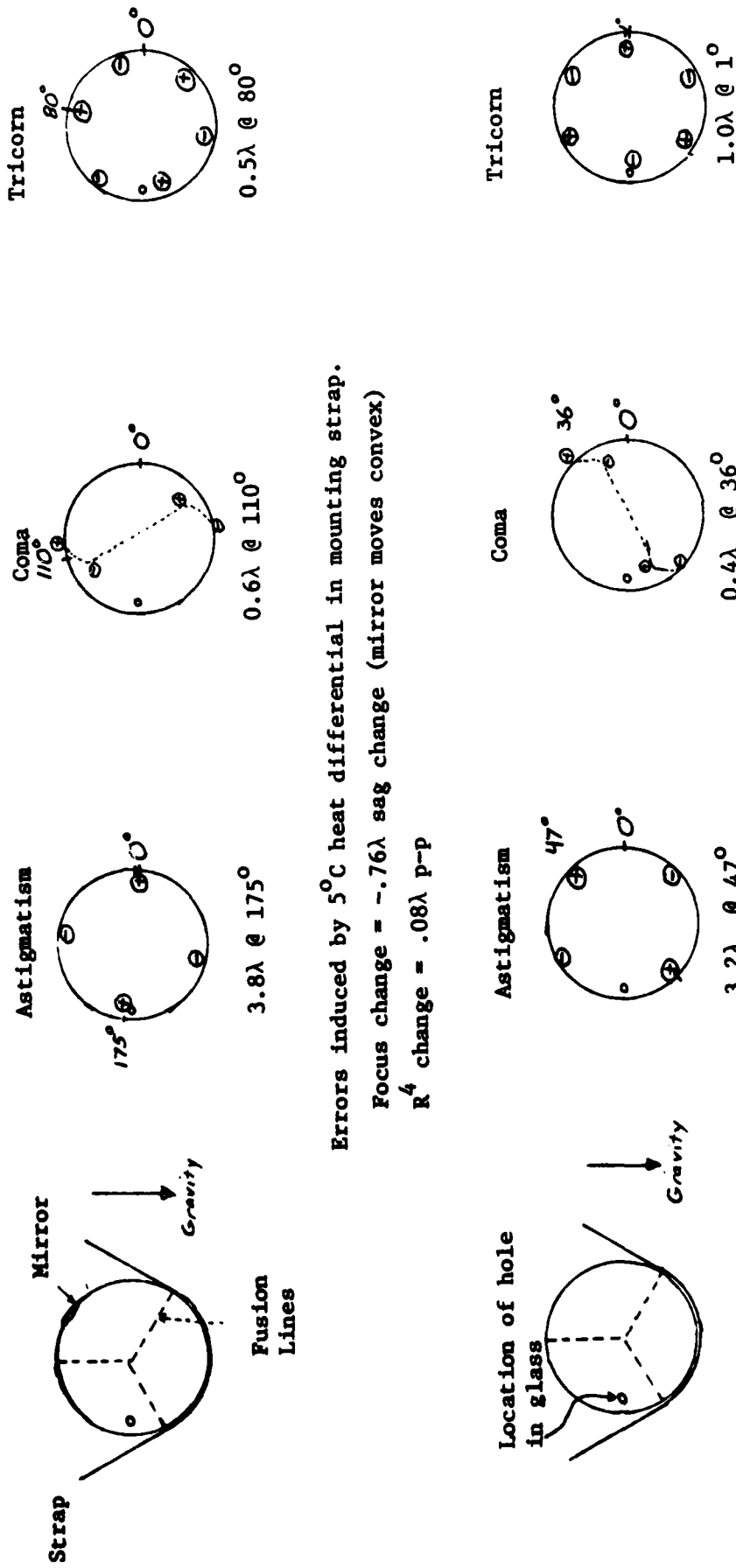


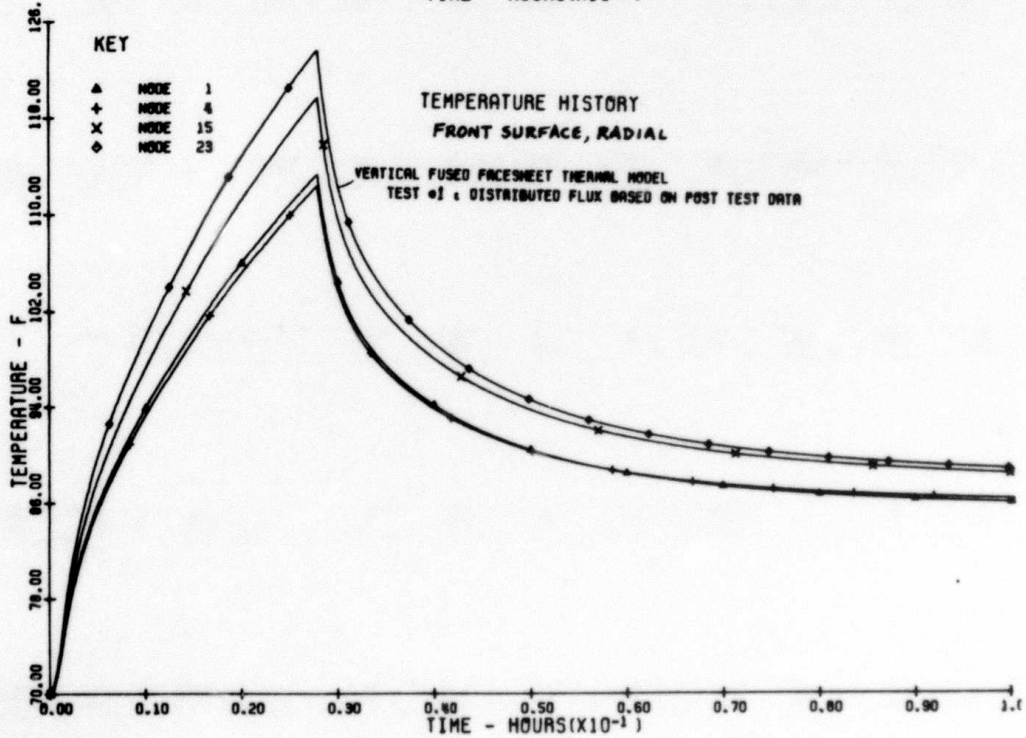
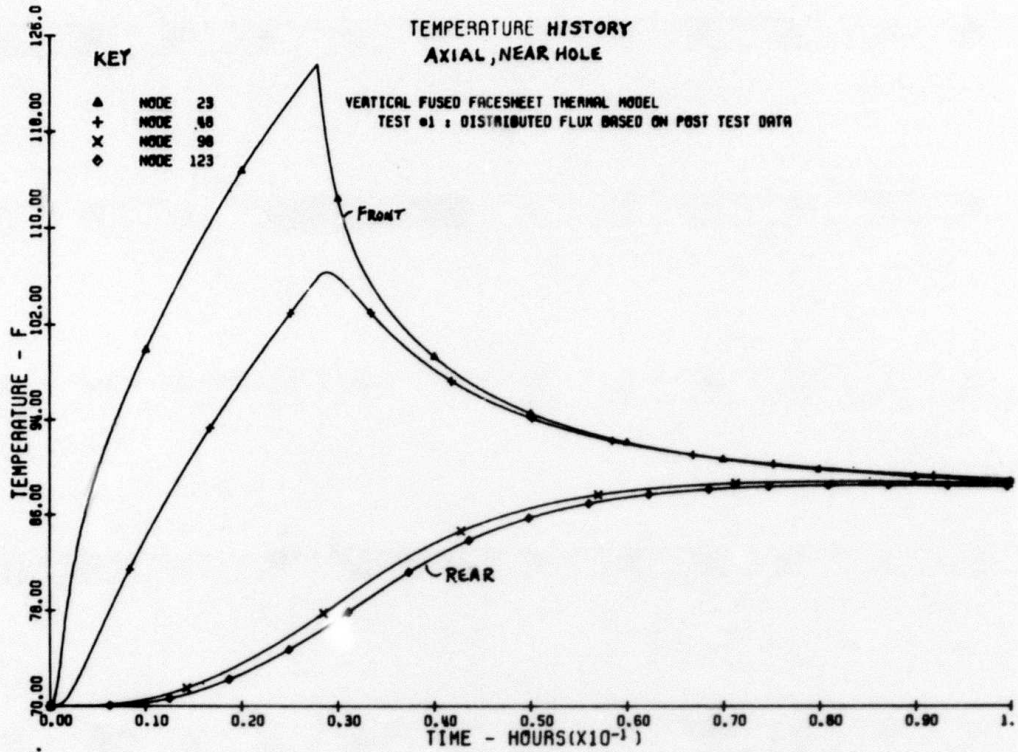
Figure 3 Mount Effects

NO.	DECK	FIT TYPE	SCALE	RMS	PK-PK	FDCLS	BLUR FOCUS	FOC INCL. SPHERICAL	CYLINDER AMT.	CYLINDER ANG.	COMA AMT.	COMA ANG.	TRICORN AMT.	TRICORN ANG.	DR4
		NONEAR		0.0000	0.0000	0.0000	0.0000	0.0000	0.0000	0.0000	0.0000	0.0000	0.0000	0.0000	0.0000
		FOCUS		0.0000	0.0000	0.0000	0.0000	0.0000	0.0000	0.0000	0.0000	0.0000	0.0000	0.0000	0.0000
		ASTIGMATISM		0.0000	0.0000	0.0000	0.0000	0.0000	0.0000	0.0000	0.0000	0.0000	0.0000	0.0000	0.0000
		TRICORN		0.0000	0.0000	0.0000	0.0000	0.0000	0.0000	0.0000	0.0000	0.0000	0.0000	0.0000	0.0000
	20 sec	TRICORN		0.0000	0.0000	0.0000	0.0000	0.0000	0.0000	0.0000	0.0000	0.0000	0.0000	0.0000	0.0000
		TRICORN		0.0000	0.0000	0.0000	0.0000	0.0000	0.0000	0.0000	0.0000	0.0000	0.0000	0.0000	0.0000
		TRICORN		0.0000	0.0000	0.0000	0.0000	0.0000	0.0000	0.0000	0.0000	0.0000	0.0000	0.0000	0.0000
		TRICORN		0.0000	0.0000	0.0000	0.0000	0.0000	0.0000	0.0000	0.0000	0.0000	0.0000	0.0000	0.0000
	40 sec	TRICORN		0.0000	0.0000	0.0000	0.0000	0.0000	0.0000	0.0000	0.0000	0.0000	0.0000	0.0000	0.0000
		TRICORN		0.0000	0.0000	0.0000	0.0000	0.0000	0.0000	0.0000	0.0000	0.0000	0.0000	0.0000	0.0000
		TRICORN		0.0000	0.0000	0.0000	0.0000	0.0000	0.0000	0.0000	0.0000	0.0000	0.0000	0.0000	0.0000
		TRICORN		0.0000	0.0000	0.0000	0.0000	0.0000	0.0000	0.0000	0.0000	0.0000	0.0000	0.0000	0.0000
	60 sec	TRICORN		0.0000	0.0000	0.0000	0.0000	0.0000	0.0000	0.0000	0.0000	0.0000	0.0000	0.0000	0.0000
		TRICORN		0.0000	0.0000	0.0000	0.0000	0.0000	0.0000	0.0000	0.0000	0.0000	0.0000	0.0000	0.0000
		TRICORN		0.0000	0.0000	0.0000	0.0000	0.0000	0.0000	0.0000	0.0000	0.0000	0.0000	0.0000	0.0000
		TRICORN		0.0000	0.0000	0.0000	0.0000	0.0000	0.0000	0.0000	0.0000	0.0000	0.0000	0.0000	0.0000
	80 sec	TRICORN		0.0000	0.0000	0.0000	0.0000	0.0000	0.0000	0.0000	0.0000	0.0000	0.0000	0.0000	0.0000
		TRICORN		0.0000	0.0000	0.0000	0.0000	0.0000	0.0000	0.0000	0.0000	0.0000	0.0000	0.0000	0.0000
		TRICORN		0.0000	0.0000	0.0000	0.0000	0.0000	0.0000	0.0000	0.0000	0.0000	0.0000	0.0000	0.0000
		TRICORN		0.0000	0.0000	0.0000	0.0000	0.0000	0.0000	0.0000	0.0000	0.0000	0.0000	0.0000	0.0000
	100 sec	TRICORN		0.0000	0.0000	0.0000	0.0000	0.0000	0.0000	0.0000	0.0000	0.0000	0.0000	0.0000	0.0000
		TRICORN		0.0000	0.0000	0.0000	0.0000	0.0000	0.0000	0.0000	0.0000	0.0000	0.0000	0.0000	0.0000
		TRICORN		0.0000	0.0000	0.0000	0.0000	0.0000	0.0000	0.0000	0.0000	0.0000	0.0000	0.0000	0.0000
		TRICORN		0.0000	0.0000	0.0000	0.0000	0.0000	0.0000	0.0000	0.0000	0.0000	0.0000	0.0000	0.0000

APPENDIX B Analytical Results for Low Flux Case, FRED Optics Summary  
(to convert angles to test angles; add 330°)



APPENDIX C Analytical Temperature Histories for Test 1



addresses	number of copies
Capt Doris Hamill RADC/OCSE	5
RADC/TSLD GRIFFISS AFB NY 13441	1
RADC/DAP GRIFFISS AFB NY 13441	2
ADMINISTRATOR DEF TECH INF CTR ATTN: DTIC-DDA CAMERON STA BG 5 ALEXANDRIA VA 22314	12
Attn: Harry Simmons Itek Corp Optical Systems Division 10 Maguire Rd Lexington, MA 02173	5
AFWL/ALAO Attn: Dr. William Lowrey Kirtland AFB, NM 87117	1
AFWL/ARAA Attn: Dr. J. Fender Kirtland AFB, NM 87117	1
ARFW/ARAA Attn: Dr. L. Skulnyk Kirtland AFB, NM 87117	1

The Aerospace Corp  
Attn: Dr. E.W. Silvertooth  
Bldg 110 MS 2339  
PO Box 92957  
Los Angeles, CA 90009

The Aerospace Corp  
Attn: T. Taylor  
Bldg 115 Room 1334C  
PO Box 92957  
Los Angeles, CA 90009

Analytic Decisions Inc  
Attn: Emmanuel Goldstein  
1401 Wilson Blvd  
Arlington, VA 22209

BDM Corp  
Attn: E. Brunson  
1820 Randolph Rd  
Albuquerque, NM 87106

BMD/ATC  
Attn: A. Carmichael  
PO Box 1500  
Huntsville, AL 35807

Boeing Aerospace Co.  
Attn: B. Allasina  
PO Box 3999  
Seattle, WA 98124

Charles Starke Draper Labs  
Attn: Frank Scammel  
555 Technology Dr.  
Cambridge, MA 02139

Charles Starke Draper Labs  
Attn: Dr. Keto Soosar  
555 Technology Dr  
MS 95  
Cambridge, MA 02139

DARPA/DEO  
Attn: Col Ronald Prater  
Arlington, VA 22209

2

Eastman Kodak  
Attn: Robert Keim  
Kodak Aparatus Division  
121 Lincoln Ave.  
Rochester, NY 14650

1

Eastman Kodak  
Attn: Richard Price  
KAD-Lincoln Park  
901 Elmgrove RD  
Rochester, NY 14650

1

GRC  
Attn: G. Gurski  
7655 Old Springhouse RD  
McLean, VA 22102

1

Itek Corp  
Attn: Roland Plante  
Optical Systems Division  
10 Maguire Rd.  
Lexington, MA 02173

1

Lockheed Palo Alto Research Lab  
Attn: Richard Feaster  
0/52-03, B201  
3251 Hanover St.  
Palo Alto, CA 94304

1

Lockheed Space and Missile Co.  
Attn: Dennis Aspinwall  
Dept 5203 Bldg. 201  
3251 Hanover St.  
Palo Alto, CA 94304

1

Lockheed Space and Missile Co.  
Attn: Dick Wallner  
Dept 5203 Bldg 201  
3251 Hanover St.  
Palo Alto, CA 94304

1

Martin Marietta Aerospace  
Attn: C.W. Spieth  
Denver Division  
PO Box 179  
Denver, CO 80201

MIT/Lincoln Laboratory  
Attn: Alex Parker  
PO Box 73  
Lexington, MA 02173

MRJ Corp  
Attn: Dr. Kenneth Robinson  
71 Blake St.  
Needham, MA 02192

NASA Ames  
Attn: James Murphy  
MS 244-7  
Moffett Field, CA 94035

NASA Marshall Space Flight Center  
Attn: Charles O. Jones  
Mail Code EC32  
Huntsville, AL 35812

Naval Sea Systems Command  
Attn: Dr. Sadeq Siahatgar  
PMS-405  
NC 1 Room 11N08  
Washington, DC 20742

Naval Weapons Center  
Attn: Dr. H. Bennett  
Code 6018  
China Lake, CA 93555

Perkin Elmer  
Attn: Dr. David Dean  
MS 241  
Main Ave  
Norwalk, CT 06856

Perkin Elmer  
Attn: Conrade Neufeld  
100 Wooster Heights Rd.  
Danbury, CT 06810

Rockwell International  
Attn: R. Brandenie  
Rocketdyne Division  
6633 Canoga Ave  
Canoga Park, CA 91304

Rockwell International  
Attn: J. Murphy  
Space Division  
12214 Lakewood Blvd  
Downey, CA 90241

Rockwell International  
Attn: R. Greenberg  
Space Division  
12214 Lakewood Blvd  
Downey, CA 90241

Riverside Research Institute  
Attn: Dr. Robert Kappesser  
1701 N Fort Myer Dr.  
Suite 711  
Arlington, VA 22209

SD/YNS  
Attn: Col H.A. Shelton  
PO Box 92960  
Worldway Postal Center  
Los Angeles, CA 90009

United Technologies Research Center  
Attn: Dr. J. Pearson  
Optics & Applied Technology Lab  
PO Box 2691  
West Palm Beach, FL 33402

University of Arizona  
Attn: Prof Robert Shannon  
\*Charles Peyton  
Administration Bldg  
Tucson, AZ 85721

W.J. Schaffer Assoc. Inc.  
Attn: Edward Borsare  
10 Lakeside Office Park  
Wakefield, MA 01880